

The Very High Energy Afterglow of Structured Jets: GW 170817 and Prospects for Future Detections

Clément Pellouin^{1,2} and Frédéric Daigne^{1,3}

¹ Sorbonne Université, CNRS, UMR 7095, Institut d’Astrophysique de Paris (IAP), 98 bis boulevard Arago, 75014 Paris, France; e-mails: pellouin@iap.fr; daigne@iap.fr

² School of Physics and Astronomy, Tel Aviv University, Tel Aviv 6997801, Israel

³ Institut Universitaire de France

Received 20 July 2023 / Accepted 11 June 2024

ABSTRACT

We present a complete numerical model of the afterglow of a laterally-structured relativistic ejecta from radio to very high energy (VHE). This includes a self-consistent calculation of the synchrotron radiation, with its maximum frequency, and of Synchrotron Self-Compton (SSC) scatterings taking into account the Klein-Nishina regime. The attenuation due to pair production is also included. This model is computationally-efficient, allowing for multi-wavelength data fitting. As a validation test, the radiative model is used to fit the broad-band spectrum of GRB 190114C at 90 s up to the TeV range. The full model is then used to fit the afterglow of GW 170817 and predict its VHE emission. We find that the SSC flux at the peak was much dimmer than the upper limit from H.E.S.S. observations. However, we show that either a smaller viewing angle or a larger external density would make similar off-axis events detectable in the future at VHE, even above 100 Mpc with the sensitivity of the CTA. Large external densities are expected in the case of fast mergers, but the existence of a formation channel for such binary neutron stars is still uncertain. We highlight that VHE afterglow detections would help probing efficiently such systems.

Key words. (Stars:) Gamma-ray burst: general – (Stars:) Gamma-ray burst: individual: GW170817 – Radiation mechanisms: non-thermal – Shock waves – Stars: neutron – Stars: binaries

1. Introduction

The first detection of gravitational waves (GW) from a Binary Neutron Star (BNS) merger, GW 170817 (Abbott et al. 2017a), was followed by several electromagnetic counterparts (Abbott et al. 2017b and references therein). A short Gamma-Ray Burst (GRB), GRB 170817A, was detected ~ 1.7 s after the GW signal (Goldstein et al. 2017; Savchenko et al. 2017); a fast-decaying thermal transient in the visible/infrared range, the kilonova, was observed for ~ 10 days after the merger (see e.g. Villar et al. 2017; Tanvir et al. 2017; Cowperthwaite et al. 2017); and a non-thermal afterglow was observed from radio to X-rays for more than three years (see e.g. Balasubramanian et al. 2021; Troja et al. 2020; Hajela et al. 2019). Among the many advances made possible by this exceptional multi-messenger event, GW 170817/GRB 170817A is in particular the first direct association between a BNS merger and a short GRB and has helped to better understand the relativistic ejection associated with such events. Indeed, the study of the relativistic ejecta benefited not only from an exceptional multi-wavelength follow-up, but also from observing conditions very different from those for other short GRBs: a much smaller distance (GW 170817 was hosted in NGC 4993 at ~ 40 Mpc, Palmese et al. 2017; Cantiello et al. 2018) and a significantly off-axis observation ($32^{+10}_{-13} \pm 1.7$ deg derived from the GW signal using the accurate localization and distance of NGC 4993, Finstad et al. 2018).

The prompt short GRB is puzzling: it is extremely weak despite the short distance, but its peak energy is above 150 keV (Goldstein et al. 2017). It is very unlikely that it is produced by internal dissipation in the ultra-relativistic core jet like in other GRBs at cosmological distance (Matsumoto et al. 2019). GRB 170817A was rather emitted in mildly-relativistic/mildly-energetic material on the line-of-sight: a promising mechanism is the shock-breakout emission when the relativistic core jet emerges from the kilonova ejecta (Bromberg et al. 2018; Gottlieb et al. 2018).

The interpretation of the afterglow is better understood. The slow rise of the light curve until its peak after $\sim 120 - 160$ days hints towards the off-axis observation of a decelerating jet surrounded by a lateral structure (see e.g. D’Avanzo et al. 2018), possibly inherited from the early interaction with the kilonova ejecta also invoked for the weak prompt emission (Gottlieb et al. 2018). The presence of a relativistic ejecta seen off-axis is confirmed by the compactness of the source and its apparent superluminal motion measured by Very Long Baseline Interferometry (VLBI) imagery (Mooley et al. 2018; Ghirlanda et al. 2019; Mooley et al. 2022). The light curve rise is dominated by the lateral structure of the relativistic ejecta, while its peak and decay are dominated by the deceleration of the ultra-relativistic core jet, which requires a kinetic energy comparable to usual values found in short GRBs (see e.g. Ghirlanda et al. 2019).

Such a lateral structure may be a common feature in GRBs due to the early propagation of the relativistic ejecta

through the infalling envelope of the stellar progenitor (long GRBs) or the post-merger ejecta responsible for the kilonova emission (short GRBs) (Bromberg et al. 2011). Possible signatures of such a lateral structure in GRBs at cosmological distance viewed slightly off-axis have been recently discussed, for instance to explain the complex phenomenology observed in the early afterglow (Beniamini et al. 2020a; Oganessian et al. 2020; Ascenzi et al. 2020; Duque et al. 2022) or the non-standard decay of the afterglow of the extremely bright GRB 221009A (O’Connor et al. 2023; Gill & Granot 2023). Accounting for the lateral structure of the jet in afterglow models has thus become necessary not only for GW 170817 but for other cosmic GRBs as well.

Most models of the off-axis afterglow of GW 170817 only consider synchrotron emission and are therefore limited to the spectral range of observations, from radio to X-rays. However, upper limits on the flux at very high energy (VHE) were obtained by H.E.S.S. at two epochs, a few days after the merger (Abdalla et al. 2017) and around its peak (Abdalla et al. 2020). Less constraining upper limits were also obtained by HAWC at early times (Galván et al. 2019) and MAGIC around the afterglow peak (Salafia et al. 2022a). Discussing the constraints associated to these upper limits requires to include the Synchrotron Self-Compton (SSC) emission in afterglow models, i.e. the Inverse Compton (IC) scatterings of the synchrotron photons by the relativistic electrons emitting them. Indeed, recent detections of the VHE afterglow of several long GRBs¹ by H.E.S.S. (GRB 180720B, Abdalla et al. 2019; GRB 190829A, H. E. S. S. Collaboration et al. 2021), MAGIC (GRB 190114C, MAGIC Collaboration et al. 2019a,b; GRB 201216C, Blanch et al. 2020) and LHAASO (GRB 221009A, LHAASO Collaboration 2023) are challenging pure synchrotron afterglow models (see however H. E. S. S. Collaboration et al. 2021) and suggests the dominant contribution of a new emission process at VHE (see the discussion of possible processes at VHE by Gill & Granot 2022), most probably SSC emission, as suggested for instance by the modelling of the afterglows of GRB 190114C (MAGIC Collaboration et al. 2019b; Wang et al. 2019; Derishev & Piran 2021), GRB 190829A (Salafia et al. 2022b) or GRB 221009A (Sato et al. 2023).

While SSC emission can be efficiently computed analytically in the Thomson regime (Panaitescu & Kumar 2000; Sari & Esin 2001), several studies have pointed out the importance to also account for the Klein-Nishina (KN) attenuation at high-energy (see e.g. Nakar et al. 2009; Murase et al. 2011; Beniamini et al. 2015; Jacovich et al. 2021; Yamasaki & Piran 2022). In the KN regime, the IC power of an electron strongly depends on its Lorentz factor. This affects the cooling of the electron distribution and therefore also impacts the synchrotron spectrum (Derishev et al. 2001; Nakar et al. 2009; Bošnjak et al. 2009), which can significantly differ from the standard prediction given by Sari et al. (1998) for the pure synchrotron case.

Motivated by these recent advances in GRB afterglow studies, we propose in this paper a consistent model of GRB afterglow emission from a decelerating laterally-structured jet where electrons accelerated at the external forward shock radiate at all wavelengths by synchrotron emission

and SSC diffusion. The treatment of SSC in the KN regime follows the approach proposed by Nakar et al. (2009), extended to account for the maximum Lorentz factor of accelerated electrons, and the attenuation at high-energy due to pair creation. The numerical implementation of the model is optimized to be computationally-efficient. This allows to use Bayesian statistics for parameter inference. We then apply this model to the multi-wavelength observations of the afterglow of GW 170817 to understand the physical constraints brought by the H.E.S.S. upper limits and to discuss if the detection of post-merger VHE afterglows may become possible in the future, especially in the coming era of the Cerenkov Telescope Array (CTA, see Cherenkov Telescope Array Consortium et al. 2019).

The model and its assumptions are detailed in Section 2 and then tested and compared to other afterglow models in Section 3. In Section 4 we show the results obtained when fitting GW 170817’s afterglow. We discuss the predicted VHE emission in light of the H.E.S.S. upper limit. We study the conditions for future post-merger detections of VHE afterglows in Section 5 and highlight that VHE emission is favored by a larger external density compared to GW 170817, which may help probing the population of fast-merging binaries, if it exists. Our conclusions are summarized in Section 6.

2. Modelling the VHE afterglow of structured jets

Our aim is to model the GRB afterglow at all wavelengths from radio bands to the TeV range. We limit ourselves to the contribution of the forward external shock propagating in the external medium and leave to a future work the extension of the model to include the reverse shock contribution at early times. Motivated by the observations of GW 170817, we rather focus here on two other aspects: the lateral structure of the jet and the detailed calculation of the Inverse Compton spectral component, taking into account Klein-Nishina effects.

In this section we describe our model: assumptions for the structure of the initial relativistic outflow (§ 2.1), dynamics of its deceleration (§ 2.2), assumptions for the acceleration of electrons and the amplification of the magnetic field at the shock front (§ 2.3), detailed calculation of the emission in the comoving frame of the shocked external medium (including synchrotron and Inverse Compton components, § 2.4) and finally integration over equal-arrival time surfaces to compute the observed flux in the observer frame (light curves and spectra, § 2.5). Our numerical implementation of this model optimizes the computation time (typically a few seconds to compute light curves and/or spectra at different frequencies on a laptop) so that we can explore the parameter space with a Bayesian approach for data fitting, as described in Section 4. In the following, in case of ambiguity, a physical quantity q is written q without a prime in the fixed source frame, and q' with a prime in the comoving frame of the emitting material.

2.1. Relativistic outflow: geometry and structure

We consider a laterally-structured jet. The initial energy per solid angle $\epsilon_0(\theta)$ and the initial Lorentz factor $\Gamma_0(\theta)$ decrease with θ , the angle from the jet axis. We define θ_c as the opening angle of the core, i.e. the ultra-relativistic/ultra-

¹ Candidate VHE photons are associated at a lower level of confidence with several other bursts by MAGIC, including the short GRB 160821B (Acciari et al. 2021).

energetic central part of the jet. We then express

$$\epsilon_0(\theta) = \epsilon_0^c \times f_a \left(\frac{\theta}{\theta_c} \right) \quad (1)$$

and

$$\Gamma_0(\theta) = 1 + (\Gamma_0^c - 1) \times g_b \left(\frac{\theta}{\theta_c} \right), \quad (2)$$

where ϵ_0^c is the initial energy per solid angle and Γ_0^c is the initial Lorentz factor, both on the jet axis ($\theta = 0$). f_a and g_b are the normalized profiles for the energy and Lorentz factor in the lateral structure.

Different lateral structures have been suggested in the literature, following the photometric and VLBI observations of GW 170817's GRB afterglow. In this paper, we model this afterglow assuming the power-law structure used by [Duque et al. \(2019\)](#):

$$f_a(x) = \begin{cases} 1 & \text{if } x < 1 \\ x^{-a} & \text{if } x \geq 1 \end{cases}, \quad (3)$$

$$g_b(x) = \begin{cases} 1 & \text{if } x < 1 \\ x^{-b} & \text{if } x \geq 1 \end{cases}. \quad (4)$$

This prescription allows a direct comparison with a top-hat jet ($f_a(x) = g_b(x) = 1$ for $x \leq 1$ and 0 otherwise). For comparison with other studies (see Section 3), we also considered the following possible structures:

- Power-law jet from [Gill & Granot \(2018\)](#): $f_a(x) = X^{-a}$ and $g_b(x) = X^{-b}$, with $X = \sqrt{1 + x^2}$.
- Power-law jet as defined in `afterglowpy`, from [Ryan et al. \(2020\)](#): $f_a(x) = \left(\sqrt{1 + x^2/a} \right)^{-a}$. The model used in `afterglowpy` is limited to the self-similar evolution of the jet, which is independent of the initial value of the Lorentz factor. Therefore g_b is not specified in this case.
- Gaussian jet from [Gill & Granot \(2018\)](#): $f_a(x) = g_b(x) = \max \left(e^{-x^2/2}; e^{-x_{\max}^2/2} \right)$, where $x_{\max} = \theta_{\max}/\theta_c$ and θ_{\max} is defined as the angle where $\beta_{0,\min}(\theta_{\max}) = 0.01$ (by default) or any other specific value. We note that [Ryan et al. \(2020\)](#) use a similar parametrization of the lateral structure for Gaussian jets in `afterglowpy`, with $\theta_{\max} = 90$ deg.

The initial total energy of the jet and of its core are given by

$$E_0 = 2 \int_0^{\pi/2} \epsilon_0(\theta) 2\pi \sin \theta \, d\theta, \quad (5)$$

$$E_0^c = 2 \int_0^{\theta_c} \epsilon_0(\theta) 2\pi \sin \theta \, d\theta. \quad (6)$$

The factor 2 accounts for the counter-jet. The usual isotropic-equivalent energy of the core jet equals

$$E_{0,\text{iso}}^c = \frac{E_0^c}{1 - \cos \theta_c}. \quad (7)$$

For the power-law structure considered here (Equation 3), we have $E_0^c = 4\pi\epsilon_0^c (1 - \cos \theta_c)$ and $E_{0,\text{iso}}^c = 4\pi\epsilon_0^c$.

We do not consider in this paper a possible radial structure of the outflow that may also very well be present due

to the variability of the central engine. This radial structure may be at least partially smoothed out during the early propagation, e.g. via internal shocks ([Kobayashi et al. 1997](#); [Daigne & Mochkovitch 1998, 2000](#)) and should have more impact on the reverse shock (see e.g. [Uhm & Beloborodov 2007](#); [Genet et al. 2007](#)), not included in the present version of the model. Therefore $E_{0,\text{iso}}^c$, Γ_0^c , θ_c , a and b (or $\beta_{0,\min}$ for the Gaussian jet) are the only four free parameters needed to fully describe the initial structure of the jet before the deceleration starts.

In our numerical implementation of the model, we suppress the lateral structure above the maximum angle θ_{\max} . This angle is taken as the maximum between θ_ϵ , defined as the angle up to which a fraction $(1 - \epsilon)$ of the jet energy is contained, and the viewing angle θ_v (see § 2.5). We therefore solve for θ_ϵ the equation

$$(1 - \epsilon)E_0 = 2 \int_0^{\theta_\epsilon} \epsilon_0(\theta) 2\pi \sin \theta \, d\theta. \quad (8)$$

We use $\epsilon = 0.01$ in the following. [Ryan et al. \(2020\)](#) introduce a similar parameter θ_W , to minimize computation time. Taking $\theta_{\max} = \max(\theta_\epsilon; \theta_v)$ allows to keep a precise calculation at early times even for very large viewing angles.

In practice, the lateral structure is discretized in $N + 1$ components, $i = 0$ being the core jet and $i = 1 \rightarrow N$ being rings at increasing angles in the lateral structure. Each component is defined by $\theta_{\min,i} \leq \theta \leq \theta_{\max,i}$ with $\theta_{\min,0} = 0$ and $\theta_{\max,0} = \theta_c$ for the core jet; $\theta_{\min,i} = \theta_{\max,i-1}$ for $i = 1 \rightarrow N$ and $\theta_{\max,N} = \theta_{\max}$. Each component is treated independently with fixed limits in latitude (no lateral spreading). The dynamics is computed such that $R_i(t) = R(\theta_i; t)$ and $\Gamma_i(t) = \Gamma(\theta_i; t)$, where $R(\theta, t)$ and $\Gamma(\theta, t)$ are given by the solution for the dynamics of the deceleration discussed below, and where $\theta_i = (\theta_{\min,i} + \theta_{\max,i})/2$ for $i \geq 1$ and $\theta_0 = 0$. We define the successive $\theta_{\min,i}$ and $\theta_{\max,i}$ such that each component carries an equal amount of energy (except for the core, $i = 0$), though a linear increase can also be chosen. Finally, we typically choose a discretization comprised of $N = 15$ components, that we find to be a good compromise between model accuracy and computational efficiency.

2.2. Dynamics of the deceleration

The structured outflow decelerates in an external medium, with an assumed density profile as a function of radius R :

$$\rho_{\text{ext}}(R) = \frac{A}{R^s}, \quad (9)$$

with $s = 0$ for a constant-density external medium as considered in the following to model the afterglow of GW 170817. In this case we write $A = n_{\text{ext}} m_p$ with n_{ext} the external medium density. We focus on the dynamics of the shocked external medium at the forward shock. It is computed assuming that (i) the dynamics of each ring of material at angle θ is independent of other angles; (ii) the lateral expansion of the outflow is negligible. These two assumptions are questionable at late times, close to the transition to the Newtonian regime ([Rhoads 1997](#)).

The Lorentz factor $\Gamma(\theta; R)$ of the shocked material at angle θ and radius R is computed in a simplified way, using energy conservation (see e.g. [Panaitescu & Kumar 2000](#);

Gill & Granot 2018):

$$\Gamma(\theta; R) = \frac{\Gamma_0(\theta)}{2m(\theta; R)} \times \left[-1 + \sqrt{1 + 4m(\theta; R) + 4 \left(\frac{m(\theta; R)}{\Gamma_0(\theta)} \right)^2} \right], \quad (10)$$

where

$$m(\theta; R) = \frac{M_{\text{ext}}(R)}{M_{\text{ej}}(\theta)/\Gamma_0(\theta)} = \left(\frac{R}{R_{\text{dec}}(\theta)} \right)^{3-s}, \quad (11)$$

with $M_{\text{ext}}(R) = \int_0^R \rho_{\text{ext}}(R) R^2 dR$ the swept-up mass per unit solid angle and $M_{\text{ej}}(\theta) = \epsilon_0(\theta)/\Gamma_0(\theta)c^2$ the ejected mass per unit solid angle. The deceleration radius of the material at angle θ is defined by

$$R_{\text{dec}}(\theta) = \left(\frac{(3-s)\epsilon_0(\theta)}{4\Gamma_0^2(\theta)c^2} \right)^{1/(3-s)}. \quad (12)$$

For a power-law structure as defined by Equations (3–4), the deceleration radius scales as $R_{\text{dec}}(\theta) \propto \theta^{\frac{2b-a}{3-s}}$. Best-fit models of the afterglow of GW 170817 usually have $2b > a$ so that the deceleration radius is larger at high latitude (see § 4.2). More generally, Beniamini et al. (2020b) derived the conditions for the observed afterglow light curve to have a single peak, as in the case of GW 170817. For an off-axis observation with a large viewing angle, these conditions are $\Gamma_0^c \theta_c > 1$; $2b > a/(4-s)$ (i.e. $8b > a$ for a uniform external medium); $b > -\ln \Gamma_0^c / \ln \theta_c$; and $\theta_v > \theta_c (\Gamma_0^c \theta_c)^{\frac{1}{b-1}}$.

This description allows us to characterize the early-time dynamics in the coasting phase $R \ll R_{\text{dec}}(\theta)$ where the Lorentz factor remains constant. It branches continuously to the relativistic self-similar evolution (Blandford & McKee 1976) for $R_{\text{dec}}(\theta) \ll R \ll R_N(\theta) = \Gamma_0^{\frac{2}{3-s}}(\theta) R_{\text{dec}}(\theta)$, and finally to the Sedov-Taylor phase (Sedov 1946; Taylor 1950) in the non-relativistic regime for $R \gg R_N(\theta)$. For $R \gg R_{\text{dec}}(\theta)$, the self-similar evolution becomes independent of the value of the initial Lorentz factor $\Gamma_0(\theta)$.

Once the Lorentz factor $\Gamma(\theta; R)$ and the velocity $\beta(\theta; R) = \frac{\sqrt{\Gamma^2(\theta; R) - 1}}{\Gamma(\theta; R)}$ are known, the corresponding time t in the source frame is given by

$$t(\theta; R) = \int_0^R \frac{dr}{\beta(\theta; r)c}. \quad (13)$$

This leads to the solution $R(\theta, t)$ and $\Gamma(\theta, t)$ used for the dynamics of each component of the structured jet.

The physical conditions in the shocked medium are easily deduced from the shock jump conditions in the strong shock regime (Blandford & McKee 1976). In the comoving frame, the mass density equals

$$\rho_*(\theta; R) = (4\Gamma(\theta; R) + 3) \rho_{\text{ext}}(R) \quad (14)$$

and the internal energy per unit mass is given by

$$\epsilon_*(\theta; R) = (\Gamma(\theta; R) - 1) c^2. \quad (15)$$

We assume here an adiabatic index of 4/3, valid as long as $\epsilon_* \gg c^2$. Finally, the timescale of the adiabatic cooling of the shocked region due to the spherical expansion is given in the comoving frame by

$$t'_{\text{dyn}}(\theta; R) = \frac{R}{\Gamma(\theta; R)\beta(\theta; R)c} = \frac{R}{c\sqrt{\Gamma^2(\theta; R) - 1}}. \quad (16)$$

2.3. Accelerated electrons and amplified magnetic field

We consider a shocked region where the physical conditions in the comoving frame are given by the mass density ρ_* , internal energy per unit mass ϵ_* , and dynamical timescale t'_{dyn} (i.e. characteristic timescale of the adiabatic cooling due to the spherical expansion), and we assume that the emission is produced by non-thermal shock-accelerated electrons, that radiate in a local turbulent magnetic field amplified at the shock. In practice, we consider only the forward external shock so that in this study, ρ_* , ϵ_* and t'_{dyn} are given by Equations (14–16).

We use the following standard parametrization of the microphysics at the shock: (i) a fraction ϵ_B of the internal energy is injected in the magnetic field, i.e.

$$u_B = \frac{B'^2}{8\pi} = \epsilon_B \rho_* \epsilon_*, \quad (17)$$

leading to

$$B' = \sqrt{8\pi\epsilon_B\rho_*\epsilon_*}; \quad (18)$$

(ii) a fraction ϵ_e of the internal energy is injected into non-thermal electrons, that represent a fraction ζ of all available electrons. Their number density (cm^{-3}) and energy density ($\text{erg} \cdot \text{cm}^{-3}$) in the comoving frame are therefore given respectively by

$$n_e^{\text{acc}} = \zeta \frac{\rho_*}{m_p} \quad (19)$$

and

$$u_e = \epsilon_e \rho_* \epsilon_*. \quad (20)$$

Assuming a power-law distribution at injection, with an index $-p$ and $2 < p < 3$, this leads to the following distribution of accelerated electrons (cm^{-3}):

$$n(\gamma) = (p-1) \frac{n_e^{\text{acc}}}{\gamma_m} \left(\frac{\gamma}{\gamma_m} \right)^{-p} \quad \text{for } \gamma_m \leq \gamma \leq \gamma_{\text{max}}, \quad (21)$$

where the minimum Lorentz factor at injection equals

$$\gamma_m = \frac{p-2}{p-1} \frac{\epsilon_e m_p \epsilon_*}{\zeta m_e c^2}. \quad (22)$$

As discussed later, taking into account a realistic estimate of the maximum Lorentz factor γ_{max} up to which electrons can be accelerated at the shock is important to discuss the GeV-TeV afterglow emission. This was not included in the study by Nakar et al. (2009) on which our calculation of the emission is based. Equations (21–22) above are obtained by assuming that the maximum Lorentz factor γ_{max} is much larger than γ_m . This is fully justified as we have typically $\gamma_{\text{max}}/\gamma_m > 10^6$ in the best fit models of GW 170817 at the peak (Section 4). The maximum electron Lorentz factor γ_{max} is evaluated by imposing that the acceleration timescale remains always shorter than the radiative and the dynamical timescales, i.e.

$$t'_{\text{acc}}(\gamma) \leq \min(t'_{\text{rad}}(\gamma); t'_{\text{dyn}}). \quad (23)$$

The acceleration timescale is written as a function of the Larmor time R'_L/c following Bohm's scaling,

$$t'_{\text{acc}}(\gamma) = K_{\text{acc}} \frac{R'_L(\gamma)}{c} = K_{\text{acc}} \frac{\gamma m_e c}{e B'}, \quad (24)$$

Table 1. Values of the dimensionless parameters K_P ; K_ν and $K_{P_{\max}}$ for different afterglow models used in each reference.

Reference	K_P	K_ν	$K_{P_{\max}}$
Sari et al. (1998)	1	1	1
Panaiteanu & Kumar (2000)	0.30	0.78	0.39
Sari & Esin (2001); Gill & Granot (2018)	$3.52 \frac{p-1}{3p-1}$ $\simeq 0.745$ for $p = 2.16$	$3\pi/8$ $\simeq 1.178$	$0.88 \frac{32}{3\pi} \frac{p-1}{3p-1}$ $\simeq 0.633$ for $p = 2.16$

where $K_{\text{acc}} \geq 1$ is a dimensionless factor. In practice, electrons at γ_{max} are usually fast cooling and the maximum electron Lorentz factor is determined by the radiative timescale, $t'_{\text{rad}}(\gamma)$. Its evaluation is non-trivial when Inverse Compton scatterings are taken into account (see § 2.4). The resulting detailed calculation of γ_{max} is explained in Appendix A. In the following, we assume $K_{\text{acc}} = 1$. Our value of γ_{max} should therefore be considered as an upper limit for the true value of the maximum electron Lorentz factor.

2.4. Emissivity in the comoving frame

Our calculation of the emission from non-thermal electrons is mostly taken from Nakar et al. (2009). The population of electrons cools down by adiabatic cooling, synchrotron radiation and via Synchrotron Self-Compton (SSC) scatterings. As we are interested in the VHE afterglow emission, we include in § 2.4.8 the attenuation due to pair production, without including the emission of secondary leptons. As we focus in this paper on the afterglow of GW 170817 where the radio observations do not show any evidence for absorption, we do not include in the present version of the model the effect of synchrotron self-absorption. In this subsection, all quantities are written in the comoving frame of the considered shocked region. We therefore omit the prime to simplify the notations.

2.4.1. Synchrotron and IC radiation for a single electron

Synchrotron radiation. The synchrotron power of a single electron ($\text{erg} \cdot \text{s}^{-1}$) is given by

$$P^{\text{syn}}(\gamma) = K_1 B^2 \gamma^2, \quad (25)$$

with $K_1 = K_P \frac{\sigma_T c}{6\pi}$ and K_P a dimensionless parameter, and its synchrotron frequency equals

$$\nu_{\text{syn}}(\gamma) = K_2 B \gamma^2, \quad (26)$$

with $K_2 = K_\nu \frac{e}{2\pi m_e c}$ and K_ν a dimensionless parameter. The dimensionless parameters K_P and K_ν depend on the assumptions made on the pitch angle of electrons relative to the magnetic field lines and different values are found in afterglow models, as listed in Table 1. By default, we use the same values as Gill & Granot (2018), taken from Granot et al. (1999) where they were obtained by fitting the broken power-law approximation of the synchrotron power of a power-law distribution of electrons to the exact calculation.

The corresponding synchrotron power at frequency ν ($\text{erg} \cdot \text{s}^{-1} \cdot \text{Hz}^{-1}$) is given by

$$P_\nu^{\text{syn}}(\gamma) = P_{\text{max}} \Phi\left(\frac{\nu}{\nu_{\text{syn}}(\gamma)}\right), \quad (27)$$

with

$$P_{\text{max}} = \frac{P^{\text{syn}}(\gamma)}{\nu_{\text{syn}}(\gamma)} = \frac{K_1}{K_2} B = K_{P_{\text{max}}} \frac{\sigma_T m_e c^2}{3e} B, \quad (28)$$

$K_{P_{\text{max}}} = K_P/K_\nu$ and $\int_0^\infty \Phi(x) dx = 1$. In practice we adopt a simplified shape $\Phi(x) = \frac{4}{3} x^{1/3}$ for $x \leq 1$ and 0 otherwise.

Inverse Compton scatterings. The spectral number density of seed photons is n_ν^{syn} ($\text{cm}^{-3} \cdot \text{Hz}^{-1}$), assumed to result only from the synchrotron radiation of the electrons on which they also scatter (SSC). The IC power of an electron ($\text{erg} \cdot \text{s}^{-1}$) is then given by

$$P^{\text{SSC}}(\gamma) = \int_0^\infty d\nu n_\nu^{\text{syn}} \sigma_T f_{\text{KN}}(w) c K_{\text{IC}} \gamma^2 g_{\text{KN}}(w) h\nu, \quad (29)$$

where $w = \gamma h\nu/m_e c^2$; and f_{KN} and g_{KN} are the KN corrections to the cross-section and to the mean energy of the scattered photon. In the Thomson regime ($w \ll w_{\text{KN}}$), the cross-section is σ_T and the mean energy of scattered photons is $K_{\text{IC}} \gamma^2 h\nu$ for a seed synchrotron photon of frequency ν , so that $f_{\text{KN}} = g_{\text{KN}} = 1$ for $w \ll w_{\text{KN}}$. By default, we use the standard values $K_{\text{IC}} = 4/3$ and $w_{\text{KN}} = 1$, as in Nakar et al. (2009). We note however that Yamasaki & Piran (2022) recently suggested that a better agreement with a detailed numerical spectral calculation of the SSC component was achieved with $w_{\text{KN}} = 0.2$, especially at the transition between the Thomson and the KN regime. For simplicity, we do not write explicitly in Equation (29) the dependency on the angle between the upscattered photon and the scattering electron which is discussed in Nakar et al. (2009). We assume an isotropic seed radiation field. We only account for single IC scatterings as the effects of multiple scatterings are expected to be negligible since the afterglow is produced in the optically thin regime. The Compton parameter is defined by

$$Y(\gamma) = \frac{P^{\text{SSC}}(\gamma)}{P^{\text{syn}}(\gamma)}. \quad (30)$$

This Compton parameter is constant only if all SSC scatterings occur in the Thomson regime. Here we take into account the KN regime, hence the dependence to the electron Lorentz factor. This affects not only the SSC emission but also the synchrotron component. Following Nakar et al. (2009) and keeping the same notations, we simplify the IC cross-section by assuming that scatterings are entirely suppressed in the KN regime: $f_{\text{KN}}(w) = 0$ for $w \geq w_{\text{KN}}$. Then, a synchrotron photon produced by an electron with Lorentz factor γ can only be upscattered by electrons with Lorentz factors below a certain limit $\hat{\gamma}$ to remain in the Thomson regime, i.e.

$$\hat{\gamma} = \frac{w_{\text{KN}} m_e c^2}{h\nu_{\text{syn}}(\gamma)} \propto \gamma^{-2}. \quad (31)$$

Note that $\hat{\gamma}$ is a decreasing function of γ : if the energy of the synchrotron photon is higher, the maximum energy of any electron on which it could be upscattered in the Thomson

regime must be lower. In an equivalent way, electrons with Lorentz factor γ will only scatter photons below the energy

$$h\tilde{\nu} = w_{\text{KN}} m_e c^2 / \gamma. \quad (32)$$

Then it is convenient to define $\tilde{\gamma}$ such that $\nu_{\text{syn}}(\tilde{\gamma}) = \tilde{\nu}$, i.e.

$$\tilde{\gamma} = \sqrt{w_{\text{KN}} \gamma m_e c^2 / h \nu_{\text{syn}}(\gamma)} \propto \gamma^{-1/2}. \quad (33)$$

Electrons with a Lorentz factor γ can only scatter synchrotron photons produced by electrons with Lorentz factors below $\tilde{\gamma}$. The Lorentz factor γ_{self} is defined by

$$\gamma_{\text{self}} = \hat{\gamma}_{\text{self}} = \tilde{\gamma}_{\text{self}} = \left(\frac{w_{\text{KN}} m_e c^2}{h K_2 B} \right)^{1/3}. \quad (34)$$

The definition of $\tilde{\nu}$ allows to simplify the expression of the SSC power given by Equation (29):

$$P^{\text{SSC}}(\gamma) = K_{\text{IC}} \sigma_{\text{T}} c \gamma^2 \int_0^{\tilde{\nu}} d\nu u_{\nu}^{\text{syn}}, \quad (35)$$

with $u_{\nu}^{\text{syn}} = n_{\nu}^{\text{syn}} \times h\nu$ the energy density of the seed synchrotron photons ($\text{erg} \cdot \text{cm}^{-3} \cdot \text{Hz}^{-1}$). Then

$$Y(\gamma) = \frac{3 K_{\text{IC}} \int_0^{\tilde{\nu}} d\nu u_{\nu}^{\text{syn}}}{4 K_{\text{P}} u_{\text{B}}}. \quad (36)$$

Assuming a strict suppression in the KN regime leads to a simple expression for the SSC power at frequency ν ($\text{erg} \cdot \text{s}^{-1} \cdot \text{Hz}^{-1}$) for a single electron of Lorentz factor γ :

$$P_{\nu}^{\text{SSC}}(\gamma) = \sigma_{\text{T}} c u_{\nu_{\text{seed}}=\nu/(K_{\text{IC}}\gamma^2)}^{\text{syn}} \quad (37)$$

if $h\nu \leq K_{\text{IC}} \gamma m_e c^2$ and 0 otherwise.

2.4.2. Radiative regime of a single electron

Following Sari et al. (1998), the first expected break in the electron distribution occurs at the critical electron Lorentz factor γ_c , defined by the condition $t_{\text{rad}}(\gamma) = t_{\text{dyn}}$, so that high-energy electrons with $\gamma \gg \gamma_c$ are radiatively efficient (fast cooling), and low-energy electrons with $\gamma \ll \gamma_c$ are mainly cooling via the adiabatic expansion and are radiatively inefficient (slow cooling). The radiative timescale is given by

$$t_{\text{rad}}(\gamma) = \frac{\gamma m_e c^2}{P_{\text{syn}}(\gamma) + P_{\text{SSC}}(\gamma)} = \frac{m_e c^2}{[1 + Y(\gamma)] K_1 B^2 \gamma}. \quad (38)$$

Then, computing self-consistently γ_c requires to solve the equation

$$\gamma_c [1 + Y(\gamma_c)] = \gamma_c^{\text{syn}} = \frac{m_e c^2}{K_1 B^2 t_{\text{dyn}}}, \quad (39)$$

where γ_c^{syn} is the value of the critical Lorentz factor obtained when only taking into account the synchrotron radiation. Our procedure to compute γ_c and $Y(\gamma_c)$ in the most general case where the SSC cooling impacts the electron distribution is discussed below in § 2.4.6.

2.4.3. Electron distribution and associated emission

Electron distribution. Following Nakar et al. (2009), we compute the time-averaged distribution of electrons $\bar{n}(\gamma)$ over the dynamical timescale t_{dyn} by keeping only the dominant term for the electron cooling: the instantaneous power of an electron is either dominated by the synchrotron and SSC radiation $(1 + Y(\gamma)) P^{\text{syn}}(\gamma)$ for $\gamma > \gamma_c$ or the adiabatic cooling $\gamma m_e c^2 / t_{\text{dyn}}$ if $\gamma < \gamma_c$. This leads to

$$\bar{n}(\gamma) = \frac{n_e^{\text{acc}}}{1 + Y(\gamma)} \frac{\gamma_c^{\text{syn}}}{\gamma_m^2} \times \begin{cases} (\gamma/\gamma_m)^{-2} & \text{if } \gamma_c < \gamma < \gamma_m \\ (\gamma/\gamma_m)^{-(p+1)} & \text{if } \gamma_m < \gamma < \gamma_{\text{max}} \end{cases} \quad (40)$$

in fast cooling regime ($\gamma_m > \gamma_c$) and

$$\bar{n}(\gamma) = n_e^{\text{acc}} \frac{\gamma_c^{\text{syn}}}{\gamma_m^2} \left(\frac{\gamma_c}{\gamma_m} \right)^{-(p+1)} \times \begin{cases} (\gamma/\gamma_c)^{-p} / (1 + Y(\gamma_c)) & \text{if } \gamma_m < \gamma < \gamma_c \\ (\gamma/\gamma_c)^{-(p+1)} / (1 + Y(\gamma)) & \text{if } \gamma_c < \gamma < \gamma_{\text{max}} \end{cases} \quad (41)$$

in slow cooling regime ($\gamma_m < \gamma_c$). We define $\gamma_{m,c} = \max(\gamma_m; \gamma_c)$ and $\gamma_{c,m} = \min(\gamma_m; \gamma_c)$ so that $\gamma_{m,c} = \gamma_m$ and $\gamma_{c,m} = \gamma_c$ in fast cooling and $\gamma_{m,c} = \gamma_c$ and $\gamma_{c,m} = \gamma_m$ in slow cooling. The minimum electron Lorentz factor is therefore $\gamma_{\text{min}} = \gamma_{c,m}$. We define the corresponding synchrotron frequencies $\nu_{m,c} = \nu_{\text{syn}}(\gamma_{m,c})$ and $\nu_{c,m} = \nu_{\text{syn}}(\gamma_{c,m})$. We also always keep only the dominant term in the radiated power, i.e. $1 + Y(\gamma) \simeq 1$ if $Y(\gamma) < 1$ and $Y(\gamma)$ otherwise. As described in detail in Nakar et al. (2009), the resulting distribution shows several breaks in addition to γ_m and γ_c : a break is expected at γ_0 such that $Y(\gamma_0) = 1$ and several additional breaks are possible and must be identified in an iterative way, as described in § 2.4.6.

Following Sari et al. (1998) and Nakar et al. (2009), we approximate $\bar{n}(\gamma)$ and the associated synchrotron spectrum by broken power-laws to allow for a semi-analytical calculation. Electrons Lorentz factors are normalized by $\gamma_{m,c}$, i.e. $x = \gamma/\gamma_{m,c}$, and photon frequencies by $\nu_{m,c}$, i.e. $y = \nu/\nu_{m,c}$. Hence the normalized synchrotron frequency of an electron with normalized Lorentz factor x is $y = x^2$. In the following the notations introduced for characteristic electron Lorentz factors or photon frequencies are implicitly conserved for the normalized quantities. For instance $x_{\text{self}} = \gamma_{\text{self}}/\gamma_{m,c}$, $\hat{x} = \tilde{\gamma}/\gamma_{m,c} = x_{\text{self}}^3/x^2$, $\tilde{y} = \tilde{\nu}/\nu_{m,c} = \tilde{x}^2$, etc.

Normalized electron distribution. The electron distribution is given by

$$\bar{n}(\gamma) = \frac{1}{I_0} \frac{n_e^{\text{acc}}}{\gamma_{m,c}} f(x), \quad (42)$$

where $f(x)$ is the normalized broken power-law electron distribution with N breaks and power-law segments:

$$f(x) = \begin{cases} x^{-p_1} & \text{if } x_1 \leq x \leq x_2 \\ x_2^{p_2-p_1} x^{-p_2} & \text{if } x_2 \leq x \leq x_3 \\ x_2^{p_2-p_1} x_3^{p_3-p_2} x^{-p_3} & \text{if } x_2 \leq x \leq x_3 \\ \vdots & \vdots \\ x_2^{p_2-p_1} x_3^{p_3-p_2} \dots x_N^{p_N-p_{N-1}} x^{-p_N} & \text{if } x_N \leq x \leq x_{N+1} \end{cases} \quad (43)$$

with $x_1 = \gamma_{\text{min}}/\gamma_{m,c}$ and $x_{N+1} = \gamma_{\text{max}}/\gamma_{m,c}$. The number of breaks in the pure synchrotron case or if all IC scatterings are in the Thomson regime is $N = 2$, as discussed in

§ 2.4.4 and 2.4.5. In the general case where KN corrections cannot be neglected, more breaks appear in the electron distribution as discussed in § 2.4.6. All possible cases are provided in Appendix B. Typically, $N = 2$ to 5, except in some very specific regions of the parameter space (case III in Nakar et al. 2009), also discussed in Appendix B.

The dimensionless integral I_0 is given by

$$I_0 = \int_{x_1}^{x_{N+1}} f(x) dx, \quad (44)$$

to conserve the number of electrons: $\int_{\gamma_{\min}}^{\gamma_{\max}} \bar{n}(\gamma) d\gamma = n_e^{\text{acc}}$.

Normalized synchrotron spectrum. The synchrotron power per electron and per unit frequency p_ν^{syn} ($\text{erg} \cdot \text{s}^{-1} \cdot \text{Hz}^{-1} \cdot \text{electron}^{-1}$) averaged over the timescale t_{dyn} is deduced from Equation (27) using the simplified shape for Φ . This leads to a broken power-law synchrotron spectrum:

$$\begin{aligned} p_\nu^{\text{syn}} &= \frac{1}{n_e^{\text{acc}}} \int_{\gamma_{\min}}^{\gamma_{\max}} d\gamma \bar{n}(\gamma) P_\nu^{\text{syn}}(\gamma) \\ &= \frac{\gamma_{\text{m,c}}^2 m_e c^2}{\gamma_c^{\text{syn}} \nu_{\text{m,c}} t_{\text{dyn}}} \times \frac{4}{3} y^{1/3} \int_{\max(x_1, y^{1/2})}^{x_{N+1}} dx \frac{f(x)}{x^{2/3}} \\ &\simeq \frac{1}{I_0} \frac{I_2}{J_0} \frac{\gamma_{\text{m,c}}^2 m_e c^2}{\gamma_c^{\text{syn}} \nu_{\text{m,c}} t_{\text{dyn}}} \times g(y), \end{aligned} \quad (45)$$

where the normalized broken power-law spectral shape is obtained by keeping the dominant term in the integral of $f(x)/x^{2/3}$, i.e.

$$g(y) = \begin{cases} x_1^{\frac{1}{3}-p_1} y^{\frac{1}{3}} & \text{if } y < x_1^2 \\ y^{-\frac{p_1-1}{2}} & \text{if } x_1^2 < y < x_2^2 \\ x_2^{p_2-p_1} y^{-\frac{p_2-1}{2}} & \text{if } x_2^2 < y < x_3^2 \\ x_2^{p_2-p_1} x_3^{p_3-p_2} y^{-\frac{p_3-1}{2}} & \text{if } x_3^2 < y < x_4^2 \\ \vdots & \vdots \\ x_2^{p_2-p_1} x_3^{p_3-p_2} \dots x_N^{p_N-p_{N-1}} y^{-\frac{p_N-1}{2}} & \text{if } x_N^2 < y < x_{N+1}^2 \end{cases} \quad (46)$$

The dimensionless factors I_2 and J_0 are defined by

$$I_2 = \int_{x_1}^{x_{N+1}} dx x^2 f(x) \quad (47)$$

$$J_0 = \int_0^{x_{N+1}^2} dy g(y), \quad (48)$$

to ensure that the total synchrotron power per electron ($\text{erg} \cdot \text{s}^{-1} \cdot \text{electron}^{-1}$) is conserved:

$$\begin{aligned} p^{\text{syn}} &= \int_0^\infty d\nu p_\nu^{\text{syn}} = \frac{I_2}{I_0} \frac{\gamma_{\text{m,c}}^2 m_e c^2}{\gamma_c^{\text{syn}} t_{\text{dyn}}} \\ &= \frac{1}{n_e^{\text{acc}}} \int_{\gamma_{\min}}^{\gamma_{\max}} d\gamma \bar{n}(\gamma) P^{\text{syn}}(\gamma). \end{aligned} \quad (49)$$

Finally we define ν_p as the peak frequency of the synchrotron spectrum, i.e. the frequency ν where $\nu^2 p_\nu^{\text{syn}}$ is maximum. This peak frequency corresponds to synchrotron photons emitted by electrons at Lorentz factor γ_p , i.e. $\nu_p = \nu_{\text{syn}}(\gamma_p)$. We note i_p the corresponding index of the break in the normalized distributions: $x_p = x_{i_p}$ and $y_p = y_{i_p} = x_p^2$.

Normalized SSC spectrum. The SSC power per electron and per unit frequency p_ν^{SSC} ($\text{erg} \cdot \text{s}^{-1} \cdot \text{Hz}^{-1} \cdot \text{electron}^{-1}$) emitted over the timescale t_{dyn} is deduced from Equation (37) with

$$u_\nu^{\text{syn}} = n_e^{\text{acc}} p_\nu^{\text{syn}} t_{\text{dyn}}. \quad (50)$$

This leads to

$$p_\nu^{\text{SSC}} = \frac{1}{n_e^{\text{acc}}} \int_{\gamma_{\min}}^{\gamma_{\max}} d\gamma \bar{n}(\gamma) P_\nu^{\text{SSC}}(\gamma) \quad (51)$$

$$\simeq \frac{1}{I_0} \frac{I_2}{J_0} \frac{\tau_T}{I_0} \frac{\gamma_{\text{m,c}}^2 m_e c^2}{\gamma_c^{\text{syn}} \nu_{\text{m,c}} t_{\text{dyn}}} \times G(y), \quad (52)$$

where

$$\tau_T = n_e^{\text{acc}} \sigma_T c t_{\text{dyn}} \quad (53)$$

is the Thomson optical depth and where the normalized spectral shape is given by

$$G(y) = \int_{\max\left(x_1; \frac{1}{K_{\text{IC}}} \frac{h\nu_{\text{m,c}}}{\gamma_{\text{m,c}} m_e c^2} y\right)}^{x_{N+1}} dx f(x) g\left(y_{\text{seed}} = \frac{1}{K_{\text{IC}}} \frac{y}{\gamma_{\text{m,c}}^2 x^2}\right). \quad (54)$$

The cutoff at $x_{\text{KN}} = \gamma_{\text{KN}}/\gamma_{\text{m,c}}$ with $\gamma_{\text{KN}} = \frac{1}{K_{\text{IC}}} \frac{h\nu}{m_e c^2}$ is a direct consequence of the strict suppression assumed in the KN regime: the VHE flux due to the scatterings occurring in the KN regime are neglected. Yamasaki & Piran (2022) introduce a factor f_{KN} in their calculations to compensate this approximation, which we do not include here. The KN regime affects the high energy part of the emitted spectrum: above a photon energy $h\nu = K_{\text{IC}} \gamma_{\text{min}} m_e c^2$, we have $\gamma_{\text{KN}} > \gamma_{\text{min}}$ and the SSC emission is reduced. The SSC emission is even entirely suppressed ($G(y) = 0$) at very high photon energy $h\nu > K_{\text{IC}} \gamma_{\text{max}} m_e c^2$ corresponding to $\gamma_{\text{KN}} > \gamma_{\text{max}}$.

In practice, $G(y)$ is computed exactly in our numerical implementation. Note also that $J_0 \simeq 2I_2$ when only the leading term is kept in the integrals. However all dimensionless factors I_0 , I_2 and J_0 are also computed exactly in our numerical implementation, which ensures the continuity of the electron distribution and emitted spectrum at the transition from the fast to the slow cooling regime, as well as between the different possible cases in both regimes (see § 2.4.6).

2.4.4. The pure synchrotron case

The standard pure synchrotron case where the SSC emission is neglected ($Y(\gamma) = 0$ for all electrons) is fully described in Sari et al. (1998). We have $\gamma_c = \gamma_c^{\text{syn}}$ in this case. In the fast cooling regime ($\gamma_m > \gamma_c$), the normalized distributions are given by

$$f(x) = \begin{cases} x^{-2} & \text{if } x_1 < x < x_2 \\ x_2^{p-1} x^{-(p+1)} & \text{if } x_2 < x < x_3 \end{cases}, \quad (55)$$

$$g(y) = \begin{cases} x_1^{-5/3} y^{1/3} & \text{if } y < x_1^2 \\ y^{-1/2} & \text{if } x_1^2 < y < x_2^2 \\ x_2^{p-1} y^{-p/2} & \text{if } x_2^2 < y < x_3^2 \end{cases}, \quad (56)$$

with $x_1 = \gamma_c/\gamma_m$, $x_2 = 1$ and $x_3 = \gamma_{\max}/\gamma_m$. In the slow cooling regime ($\gamma_m < \gamma_c$), they are given by

$$f(x) = \begin{cases} x^{-p} & \text{if } x_1 < x < x_2 \\ x_2 x^{-(p+1)} & \text{if } x_2 < x < x_3 \end{cases}, \quad (58)$$

$$g(y) = \begin{cases} x_1^{1/3-p} y^{1/3} & \text{if } y < x_1^2 \\ y^{-(p-1)/2} & \text{if } x_1^2 < y < x_2^2 \\ x_2 y^{-p/2} & \text{if } x_2^2 < y < x_3^2 \end{cases}, \quad (59)$$

with $x_1 = \gamma_m/\gamma_c$, $x_2 = 1$ and $x_3 = \gamma_{\max}/\gamma_c$. Calculations using this prescription are labeled as "no SSC" in the following.

2.4.5. The SSC case in Thomson regime

If the KN regime is neglected, all IC scatterings occur in Thomson regime and the Compton parameter is the same for all electrons: $Y(\gamma) = Y^{\text{no KN}} = \text{cst}$. The corresponding solution is given by Sari & Esin (2001): the normalized distributions $f(x)$ and $g(y)$ are the same as in the pure synchrotron case above, but the value of the critical Lorentz factor γ_c is decreased due to the IC cooling, $\gamma_c = \gamma_c^{\text{syn}}/(1 + Y^{\text{no KN}})$. Using Equations (36), (46) and (51), we get

$$Y^{\text{no KN}} (1 + Y^{\text{no KN}}) = \frac{3 K_{\text{IC}}}{4 K_P} \frac{p-2}{p-1} \frac{\epsilon_e}{\epsilon_B} \frac{\gamma_{m,c}}{\gamma_{c,m}} \frac{I_2}{I_0}. \quad (60)$$

As I_2/I_0 is a function of $\gamma_c/\gamma_m = \gamma_c^{\text{syn}}/\gamma_m/(1 + Y^{\text{no KN}})$, this is an implicit equation to be solved numerically to obtain $Y^{\text{no KN}}$ and γ_c . The limits for $(1 + Y^{\text{no KN}}) Y^{\text{no KN}}$ are $\frac{3 K_{\text{IC}}}{4 K_P} \frac{\epsilon_e}{\epsilon_B}$ for $\gamma_m \gg \gamma_c$ and $\frac{3 K_{\text{IC}}}{4 K_P} \frac{\epsilon_e}{\epsilon_B} \frac{1}{3-p} \left(\frac{\gamma_m}{\gamma_c^{\text{syn}}}\right)^{p-2}$ for $\gamma_m \ll \gamma_c$. Calculations using this prescription are labeled as "SSC (Thomson)" in the following.

2.4.6. Self-consistent calculation of the electron distribution and the Compton parameter in the general case

Normalized Compton parameter. In the general case where the KN suppression at high energy is included, the Compton parameter $Y(\gamma)$ is a decreasing function of the electron Lorentz factor. From Equations (36), (46) and (51), we get

$$Y(\gamma) (1 + Y(\gamma_c)) = \frac{3 K_{\text{IC}}}{4 K_P} \frac{p-2}{p-1} \frac{\epsilon_e}{\epsilon_B} \frac{\gamma_{m,c}}{\gamma_{c,m}} \frac{I_2}{I_0} \frac{1}{J_0} \int_0^{\tilde{y}} dy g(y). \quad (61)$$

Note that for low Lorentz factors γ , $\tilde{\nu}$ becomes very large so that, for $\tilde{\nu} > \nu_{\text{syn}}(\gamma_{\max})$, we recover the Thomson regime, where the right-hand side of Equation (61) is formally the same as in Equation (60), even if the integrals I_0 and I_2 can be different if the normalized electron distribution $f(x)$ is different. As described in Nakar et al. (2009), when keeping only the leading term in the integral of $g(y)$, the corresponding scaling law for the Compton parameter is $Y(\gamma) = \text{cst}$ if $\tilde{\nu}$ is above the peak frequency ν_p and $Y(\gamma) \propto \gamma^{-\frac{3-\tilde{p}}{2}}$ otherwise, where \tilde{p} is the slope of electron distribution in the power-law segment of the electron distribution including $\tilde{\gamma}$. This leads us to introduce a normalized Compton parameter defined by

$$Y(\gamma) (1 + Y(\gamma_c)) = \frac{3 K_{\text{IC}}}{4 K_P} \frac{p-2}{p-1} \frac{\epsilon_e}{\epsilon_B} \frac{\gamma_{m,c}}{\gamma_{c,m}} \frac{I_2}{I_0} h(x), \quad (62)$$

where $h(x)$ follows this scaling and is normalized so that Equation (62) has the exact limit in the Thomson regime. This leads to

$$h(x) = \begin{cases} 1 & \text{if } x < \hat{x}_p \\ \frac{\hat{x}_p^{\frac{3-p_{i_p}-1}{2}}}{\hat{x}_p^{\frac{3-p_{i_p}-1}{2}}} x^{-\frac{3-p_{i_p}-1}{2}} & \text{if } \hat{x}_p < x < \hat{x}_{i_p-1} \\ \frac{\hat{x}_p^{\frac{3-p_{i_p}-1}{2}}}{\hat{x}_{i_p-1}^{\frac{p_{i_p}-1-p_{i_p}-2}{2}}} x^{-\frac{3-p_{i_p}-2}{2}} & \text{if } \hat{x}_{i_p-1} < x < \hat{x}_{i_p-2} \\ \vdots & \vdots \\ \frac{\hat{x}_p^{\frac{3-p_{i_p}-1}{2}}}{\hat{x}_{i_p-1}^{\frac{p_{i_p}-1-p_{i_p}-2}{2}}} \cdots & \cdots \\ \cdots \hat{x}_2^{\frac{p_2-p_1}{2}} x^{-\frac{3-p_1}{2}} & \text{if } \hat{x}_2 < x < \hat{x}_1 \\ \frac{\hat{x}_p^{\frac{3-p_{i_p}-1}{2}}}{\hat{x}_{i_p-1}^{\frac{p_{i_p}-1-p_{i_p}-2}{2}}} \cdots & \cdots \\ \cdots \hat{x}_2^{\frac{p_2-p_1}{2}} \hat{x}_1^{\frac{p_1}{2}-\frac{1}{6}} x^{-4/3} & \text{if } x > \hat{x}_1 \end{cases} \quad (63)$$

We recall that i_p is the index of the break corresponding to the peak frequency of the synchrotron spectrum. In most cases (see Appendix B), we have $i_p = 2$, leading to

$$h(x) = \begin{cases} 1 & \text{if } x < \hat{x}_2 \\ \frac{\hat{x}_2^{\frac{3-p_1}{2}}}{\hat{x}_2^{\frac{3-p_1}{2}}} x^{-\frac{3-p_1}{2}} & \text{if } \hat{x}_2 < x < \hat{x}_1 \\ \frac{\hat{x}_2^{\frac{3-p_2}{2}}}{\hat{x}_1^{\frac{p_1}{2}-\frac{1}{6}}} x^{-4/3} & \text{if } x > \hat{x}_1 \end{cases}. \quad (64)$$

Self-consistent solution for the normalized electron distribution. Following Nakar et al. (2009), we define² γ_0 by $Y(\gamma_0) = 1$ and assume $1 + Y(\gamma) = Y(\gamma)$ for $\gamma < \gamma_0$ and 1 otherwise. From Equations (40) and (41), this shows that the IC cooling will only affect the electron distribution in the interval

$$\max(\gamma_c; \hat{\gamma}_p) < \gamma < \gamma_0. \quad (65)$$

Therefore the solution is entirely determined by the orderings of γ_m , γ_c , γ_0 , $\hat{\gamma}_m$ and $\hat{\gamma}_c$. All possible cases and the corresponding solutions are listed in Appendix B. In some cases, subcases are introduced as breaks can appear at $\hat{\gamma}_0$, $\hat{\gamma}_m$, $\hat{\gamma}_c$, etc. All the most relevant cases for GRB afterglows are already described in Nakar et al. (2009) along with the detailed method to obtain the corresponding solution for the electron distribution. For completeness, we list in Appendix B the additional cases allowing to fully describe the parameter space, even in regions unlikely to be explored in GRBs.

Calculation of the critical Lorentz factor γ_c . From Equation (62), we get the following equation for $Y(\gamma_c)$:

$$Y(\gamma_c) = \begin{cases} A \frac{\gamma_m}{\gamma_{\text{syn}}} \frac{I_2}{I_0} h(x_c) & \text{if } \gamma_m > \gamma_c \\ A \frac{\gamma_c}{\gamma_m} \frac{I_2}{I_0} h(x_c) & \text{if } \gamma_m < \gamma_c \text{ and } Y(\gamma_c) < 1 \\ \left(A \frac{\gamma_{\text{syn}}}{\gamma_m} \frac{I_2}{I_0} h(x_c) \right)^{1/3} & \text{if } \gamma_m < \gamma_c \text{ and } Y(\gamma_c) > 1 \end{cases} \quad (66)$$

where $A = \frac{3 K_{\text{IC}}}{4 K_P} \frac{p-2}{p-1} \frac{\epsilon_e}{\epsilon_B}$ is a constant as the microphysics parameter ϵ_B , ϵ_e and p are assumed to be constant during

² As $Y(\gamma)$ is a decreasing function with a constant first segment, if $Y(\gamma) < 1$ for $\gamma < \max(\gamma_c; \hat{\gamma}_p)$, then $Y(\gamma) < 1$ for all values of γ , and γ_0 is therefore undefined. In these cases, we retrieve the "no SSC" solution.

the forward shock propagation. Note that $x_c = 1$ in the slow cooling regime $\gamma_m < \gamma_c$. A second useful relation is obtained from Equation (62) and the definition of γ_0 :

$$Y(\gamma_c) = \frac{Y(\gamma_c)}{Y(\gamma_0)} = \frac{h(x_c)}{h(x_0)}. \quad (67)$$

Then, γ_c is computed from the following implicit equation, which is solved iteratively:

$$\gamma_c = \begin{cases} \gamma_c^{\text{syn}} & \text{if } Y(\gamma_c) < 1 \\ \gamma_c^{\text{syn}}/Y(\gamma_c) & \text{if } Y(\gamma_c) > 1 \end{cases}. \quad (68)$$

We start by assuming $Y(\gamma_c) = Y^{\text{noKN}}$ as defined in § 2.4.5 and then iterate as follows:

1. Compute γ_c from Equation (68).
2. Knowing γ_m , γ_c , γ_{self} , scan the different possible cases for the ordering of γ_m , γ_c , γ_0 , $\hat{\gamma}_m$ and $\hat{\gamma}_c$ (and additional characteristic Lorentz factors for some cases) as listed in Appendix B and compute γ_0 from Equation (67), which can be analytically inverted as provided for each case in Appendix B. We stop the scan of the possible cases when the ordering of all characteristic Lorentz factors including the obtained value of γ_0 is the correct one.
3. Having identified the correct case and therefore knowing the expression of $f(x)$, compute the integrals I_0 and I_2 .
4. Compute an updated value of $Y(\gamma_c)$ from Equation (66).
5. Start a new iteration at step 1 until convergence.

We stop the procedure when the relative variation of γ_c in an iteration falls below ϵ_{tol} . We use $\epsilon_{\text{tol}} = 10^{-4}$, which is reached in most cases in less than 20 iterations. In the context of a full afterglow light curve calculation, as we expect Y to vary smoothly during the jet propagation, we use the value of $Y(\gamma_c)$ obtained at the previous step of the dynamics instead of Y^{noKN} to start the iterative procedure. Then we usually reach a convergence in only a few iterations.

2.4.7. Final calculation of the emission in the comoving frame

The self-consistent spectrum in the comoving frame, i.e. p_ν^{syn} and p_ν^{SSC} , the synchrotron and SSC powers per electron and per unit frequency averaged over the timescale t_{dyn} , can be computed by the following procedure based on the previous paragraphs:

1. The input parameters are n_e^{acc} , t_{dyn} , B , $u_e/u_B = \epsilon_e/\epsilon_B$, γ_m , and p .
2. The following quantities can be immediately deduced: γ_c^{syn} from Equation (39), γ_{self} from Equation (34), τ_T from Equation (54), and Y^{noKN} from Equation (60).
3. Then the iterative procedure described above allows to identify the spectral regime among all the possibilities listed in Appendix B, and to compute γ_c . At the end of this step, all breaks and slopes in the functions $f(x)$ and $h(x)$ are known. The corresponding integrals I_0 and I_2 are computed by a numerical integration of Equations (44) and (48).
4. The function $g(y)$ can immediately be deduced from $f(x)$, using Equation (47). The corresponding integral J_0 is computed by a numerical integration of Equation (49), and the synchrotron spectrum per electron, p_ν^{syn} , is deduced from Equation (46).
5. Finally, the function $G(y)$ is computed by an numerical integration of Equation (55) and the SSC spectrum per electron, p_ν^{SSC} , is deduced from Equation (53).

2.4.8. Pair production

At VHE, pair production $\gamma\gamma \rightarrow e^+e^-$ can start to contribute to the SSC flux depletion. We account for this mechanism by a simplified treatment, assuming an isotropic distribution of the low-energy seed photons, as for the SSC calculation, and approximating the cross-section for pair production by a Dirac function at twice the threshold of the interaction. Then, VHE photons of frequency ν can produce pairs by interacting with low-energy photons at frequency $\nu_{\text{seed}} = 2(m_e c^2)^2 / (h^2 \nu)$ and the characteristic timescale of this interaction is given by

$$t_{\gamma\gamma}(\nu) = \frac{h}{\sigma_{\text{TC}} c} \left[u_{\nu_{\text{seed}}=2\frac{(m_e c^2)^2}{h^2 \nu}} \right]^{-1}, \quad (69)$$

with $u_\nu = u_\nu^{\text{syn}} + u_\nu^{\text{SSC}} = n_e^{\text{acc}} (p_\nu^{\text{syn}} + p_\nu^{\text{SSC}}) t_{\text{dyn}}$, leading to

$$t_{\gamma\gamma}(\nu) = \frac{h}{\tau_T} \left[(p_{\nu_{\text{seed}}}^{\text{syn}} + p_{\nu_{\text{seed}}}^{\text{SSC}})_{\nu_{\text{seed}}=2\frac{(m_e c^2)^2}{h^2 \nu}} \right]^{-1}. \quad (70)$$

For very high frequencies ν , the seed photons for pair production have a low frequency and $p_{\nu_{\text{seed}}}^{\text{syn}} + p_{\nu_{\text{seed}}}^{\text{SSC}} \simeq p_{\nu_{\text{seed}}}^{\text{syn}}$. The total emitted power per electron $p_\nu = p_\nu^{\text{syn}} + p_\nu^{\text{SSC}}$ is then corrected by a factor $\frac{t_{\gamma\gamma}(\nu)}{t_{\text{dyn}}} (1 - e^{-t_{\text{dyn}}/t_{\gamma\gamma}(\nu)})$, which in practice only attenuates the SSC component at high frequency where $t_{\gamma\gamma}(\nu) \ll t_{\text{dyn}}$.

The implementation of the model allows to select the level of approximation for the SSC emission (synchrotron only, Thomson or full calculation) and to include or not the attenuation due to the pair production.

2.5. Observed flux

Once the emissivity in the comoving frame is known (§ 2.4), the flux measured by a distant observer with a viewing angle θ_v is computed by an integration over equal-arrival time surfaces, taking into account relativistic Doppler boosting and relativistic beaming, as well as the effect of cosmological redshift. This leads to the following expression of the observer frame flux density ($\text{erg} \cdot \text{s}^{-1} \cdot \text{cm}^{-2} \cdot \text{Hz}^{-1}$) measured at time t_{obs}^z and frequency ν_{obs}^z (Woods & Loeb 1999):

$$F_{\nu_{\text{obs}}^z}(t_{\text{obs}}^z) = \frac{1+z}{4\pi D_L^2} \int_0^\infty dr \int_0^\pi d\psi \int_0^{2\pi} d\phi r^2 \sin \psi \quad (71)$$

$$\times [\mathcal{D}^2(r, \psi, t) 4\pi j'_\nu(r, \psi, \phi, t)]_{t=\frac{t_{\text{obs}}^z}{1+z} + \frac{r}{c} \cos \psi},$$

where we use spherical coordinates $(r; \psi; \phi)$ with the polar axis equal to the line-of-sight, ψ and ϕ the colatitude and longitude, and the jet axis in the direction $(\psi = \theta_v, \phi = 0)$ (see Fig. 1), and where z and D_L are the redshift and the luminosity distance of the source. Note that the angle ψ differs from θ used in § 2.2 which is measured from the jet axis. The time t (source frame) and frequency ν' (comoving frame) are given by

$$t = \frac{t_{\text{obs}}^z}{1+z} + \frac{r}{c} \cos \psi \quad (72)$$

$$\nu' = (1+z) \frac{\nu_{\text{obs}}^z}{\mathcal{D}(r, \psi, t)}. \quad (73)$$

The Doppler factor is expressed as

$$\mathcal{D}(r, \psi, t) = \frac{1}{\Gamma(r, \psi, t) (1 - \beta(r, \psi, t) \cos \psi)} \quad (74)$$

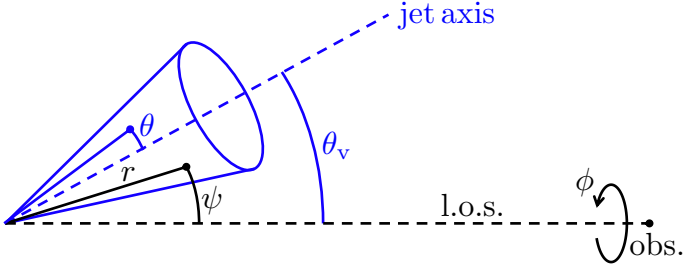


Fig. 1. Coordinates and notations used in the expression of the observed flux.

and $j'_{\nu'}$ is the emissivity ($\text{erg} \cdot \text{cm}^{-3} \cdot \text{s}^{-1} \cdot \text{Hz}^{-1} \cdot \text{sr}^{-1}$) in the comoving frame.

In practice, following the discretization of the jet structure described in § 2.1, the observer frame flux density $F_{\nu_{\text{obs}}^z}(t_{\text{obs}}^z)$ is computed as $F_{\nu_{\text{obs}}^z}(t_{\text{obs}}^z) = \sum_{i=0}^N F_{\nu_{\text{obs}}^z}^{(i)}(t_{\text{obs}}^z)$, where $F_{\nu_{\text{obs}}^z}^{(i)}(t_{\text{obs}}^z)$ are the contributions of the core jet ($i = 0$) and lateral rings ($i = 1 \rightarrow N$). To compute each contribution, the thin shell approximation allows to reduce the double integral over r and ψ in Equation (71) to a simple integral over r , or equivalently over ψ or t . In addition, to improve the computation time, the remaining integral on ϕ is computed analytically. This leads to

$$F_{\nu_{\text{obs}}^z}^{(i)}(t_{\text{obs}}^z) = \frac{1+z}{4\pi D_L^2} \int_{t_{\text{min}}^{(i)}(t_{\text{obs}}^z)}^{t_{\text{max}}^{(i)}(t_{\text{obs}}^z)} \frac{c dt}{2\Gamma_i(t) R_i(t)} \frac{\Delta\phi_i(\theta_v; \psi_i(t_{\text{obs}}^z; t))}{2\pi} \times \mathcal{D}_i^2(t_{\text{obs}}^z; t) [4\pi N_e(R_i(t))] p_{\nu'}^{(i)}(t), \quad (75)$$

where

$$\cos(\psi_i(t_{\text{obs}}^z; t)) = c \frac{t - \frac{t_{\text{obs}}^z}{1+z}}{R_i(t)}, \quad (76)$$

$$\mathcal{D}_i(t_{\text{obs}}^z; t) = \frac{1}{\Gamma_i(t) (1 - \beta_i(t) \cos \psi_i(t_{\text{obs}}^z; t))}, \quad (77)$$

$N_e(r) = \zeta M_{\text{ext}}(r)/m_p$ is the number of shock-accelerated electrons per unit solid angle, and $p_{\nu'}^{(i)}(t)$ is the power per unit frequency and per electron in the comoving frame computed in § 2.4 and evaluated at time t and comoving frequency $\nu' = (1+z)\nu_{\text{obs}}^z/\mathcal{D}_i(t_{\text{obs}}^z; t)$.

The limits of the integral $t_{\text{min}}^{(i)}(t_{\text{obs}}^z)$ and $t_{\text{max}}^{(i)}(t_{\text{obs}}^z)$ are defined by the condition $\psi_{\text{min},i} \leq \psi_i(t_{\text{obs}}^z; t) \leq \psi_{\text{max},i}$, where

$$\psi_{\text{min},i} = \begin{cases} \theta_{\text{min},i} - \theta_v & \text{if } \theta_v \leq \theta_{\text{min},i} \\ 0 & \text{if } \theta_{\text{min},i} \leq \theta_v \leq \theta_{\text{max},i} \\ \theta_v - \theta_{\text{max},i} & \text{if } \theta_{\text{max},i} \leq \theta_v \leq \pi/2 \end{cases}, \quad (78)$$

and $\psi_{\text{max},i} = \theta_v + \theta_{\text{max},i}$, i.e.

$$t - \frac{R_i(t)}{c} \cos(\psi_{\text{max},i}) \leq \frac{t_{\text{obs}}^z}{1+z} \leq t - \frac{R_i(t)}{c} \cos(\psi_{\text{min},i}). \quad (79)$$

Finally, we use the exact analytical calculation of the geometrical term $\Delta\phi_i$ defined by $\Delta\phi_i(\theta_v; \psi) = \int_0^{2\pi} d\phi f_i(\theta_v; \psi; \phi)$, where $f_i(\theta_v; \psi; \phi) = 1$ if the direction $(\psi; \phi)$ is contained in the component i (core jet or ring) and 0 otherwise.

3. Comparison with other afterglow models

3.1. Dynamics and synchrotron emission

To test our calculation of the dynamics of the forward external shock and the associated synchrotron emission, we compare our results with two other models of the afterglow of a structured jet: the model presented in Gill & Granot (2018) and `afterglowpy`, a public Python module to calculate GRB afterglow light curves and spectra, based on Ryan et al. (2020).

The first comparison is straightforward: with our default values of the normalization coefficients K_ν and K_P , the assumptions (dynamics, microphysics, radiation, calculation of observed quantities) of our model in the pure synchrotron case are exactly the same as in Gill & Granot (2018). We checked that we reproduce exactly the different cases in their Fig. 4.

The case of `afterglowpy` requires a more detailed comparison as there are differences in some treatments of the afterglow physics:

(1) Early dynamics: in `afterglowpy`, even the early-time dynamics is computed assuming the self-similar Blandford & McKee regime, i.e. $\Gamma(t; \theta) \propto E(\theta)^{1/2} n_0^{1/2} t^{-3/2}$ (see § 2.1 in Ryan et al. 2020), whereas we include the coasting phase with $\Gamma \sim \text{cst}$ before a smooth transition towards the self-similar regime at the deceleration radius, as described in § 2.2. Fig. 2 compares for a typical set of parameters the afterglow light curves from a top-hat jet viewed on-axis in radio, optical and X-rays obtained with our model (solid line), `afterglowpy` (dashed line) and our model where the dynamics has been forced to be in the self-similar regime at all times (dotted line). This allows to check that both models with the same self-similar dynamics agree well, except for the flux normalization as discussed below, and that the model with the full dynamics converge progressively towards the same solution: following the peak at the deceleration radius (at $\sim 10^{-2}$ days in this example), the light curve obtained with the full dynamics smoothly converges towards the self-similar solution, and both light curves are identical at late times (typically after the jet break at ~ 2 days in this example). On the other hand, the self-similar approximation strongly over-estimates the fluxes until the deceleration radius and the full dynamics should always be included when considering early observations (see also Wang et al. 2024). In the case of GW 170817 discussed in the next section, the earliest detection by *Chandra* was obtained ~ 9 days after the merger, by which time the core jet dynamics had reached the self-similar regime.

(2) Late dynamics: contrary to `afterglowpy`, the present version of our model does not include lateral expansion of the ejecta. When comparing with `afterglowpy`, we therefore deactivate this option in the latter, which leads to the excellent late-time agreement seen in Fig. 2. The impact of the lateral spreading is expected to be very limited as long as the core jet is relativistic (see e.g. Woods & Loeb 1999; Granot & Piran 2012; van Eerten & MacFadyen 2012; Duffell & Laskar 2018), so that we stop the jet propagation when the core Lorentz factor reaches $\Gamma = 2$ in the simulations of GW 170817's afterglow discussed in the next section. In addition, we exclude observations after 400 days from the data set used for the afterglow fitting, which corresponds to $\Gamma \gtrsim 3-4$ for the core jet in our best fit models.

(3) Flux normalization: `afterglowpy` relies on a scaling to

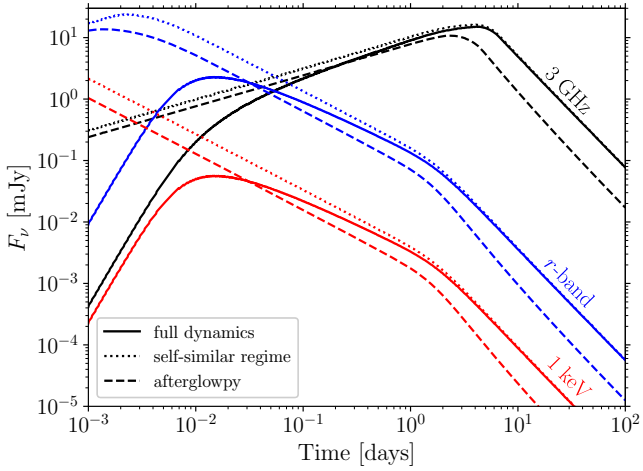


Fig. 2. Synthetic afterglow light curves of a top-hat jet viewed on-axis, in the synchrotron-only radiation regime. Solid lines show the results obtained using our model with full dynamics treatment (using Equation (10)), while dotted lines follow the self-similar solution at all times. Dashed lines are obtained with **afterglowpy** without lateral expansion. The fluxes are computed in radio at 3 GHz (black), in optical in *r*-band at 5.06×10^{14} Hz (blue) and in X-rays at 1 keV (red). The parameters used for this figure are $E_{0,\text{iso}} = 10^{52}$ erg, $\theta_c = 4$ deg, $n_{\text{ext}} = 10^{-3}$ cm $^{-3}$, $\epsilon_e = 10^{-1}$, $\epsilon_B = 10^{-1}$, $p = 2.2$, $D_L = 100$ Mpc.

boxfit (van Eerten et al. 2012), while in our model, this normalization is derived from analytical approximations detailed in Section 2. This leads to the difference of normalization seen in Fig. 2 when comparing **afterglowpy** with our model where the same self-similar dynamics is forced. The flux ratio varies between 1 and 5 at all wavelengths. When exploring a broad parameter space, varying the angle, energy injection, microphysical parameters, we checked that the flux ratio never exceeds 5.

To conclude this comparison, we note that **afterglowpy** and our model (in pure synchrotron mode) have been used by Kann et al. (2023) for two independent Bayesian inferences of the parameters of the afterglow of GRB 221009A using the same set of early observational data and converged towards very similar solutions.

3.2. Synchrotron self-Compton emission

We now test the predictions of our model in the SSC regime. Several GRBs have been observed at VHE. Two events were particularly well followed-up at all wavelengths, GRB 190114C (MAGIC Collaboration et al. 2019a,b) and GRB 221009A (LHAASO Collaboration 2023). In both cases, the VHE detection occurs at very early times but the analysis favors a dominant external forward shock origin for the emission. However, the case of GRB 221009A, which is an extreme GRB (the brightest ever detected by far) is quite complex. According to several studies, the early VHE emission and the later observations at lower frequencies probe different regions of a structured jet seen on-axis and may also include a significant contribution of the reverse shock at some frequencies (see e.g. Laskar et al. 2023; O’Connor et al. 2023; Gill & Granot 2023; Sato et al. 2023; Zheng et al. 2024; Zhang et al. 2024; Derishev & Piran 2024). We therefore decide to rather focus on GRB 190114C to test our model. This long GRB has a rich observational follow-

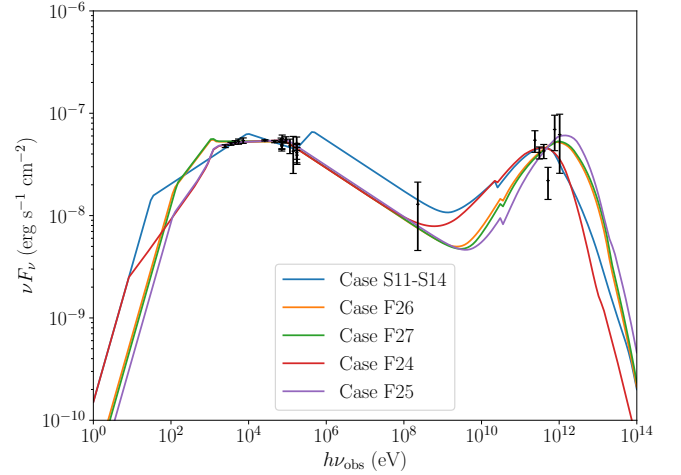


Fig. 3. Spectral fits to the afterglow observations of GRB 190114C at 90 s (black data points taken from MAGIC Collaboration et al. 2019b). Each color represents the best-fit spectrum for each of the possible radiative regimes (see text and Fig. 4). The spectral cases are detailed in Appendix B. This figure can be compared to Fig. 6 in Yamasaki & Piran (2022) showing very similar fits.

up from radio to VHE at simultaneous times. Following MAGIC Collaboration et al. (2019a), we assume that the spectrum shows two distinct components.

To test the radiative component of our model independently of the dynamics, we decide to analyse the observed spectrum at one fixed time, $t_{\text{obs}} = 90$ s, following the approach proposed by Yamasaki & Piran (2022). Their spectral model is also based on Nakar et al. (2009), which allows an easy comparison. For this purpose, we use their values $K_{\text{IC}} = 1$ and $w_{\text{KN}} = 0.2$ in this subsection. We also consider a one-zone model of the emitting region, characterized by a radius R , a Lorentz factor Γ and N_e accelerated electrons radiating in a magnetic field B' . The electrons are injected with an initial distribution with a minimum Lorentz factor γ_m and a slope p . Following Yamasaki & Piran (2022), we fix $p = 2.5$ and let four parameters free for the spectral fitting: Γ , B' , γ_m and ϵ_e/ϵ_B . Then R and t'_{dyn} are deduced from Γ and t_{obs} , n_e^{acc} from B' , ϵ_e/ϵ_B , γ_m and p , and finally N_e from n_e^{acc} , R and Γ (see Section 2 in Yamasaki & Piran 2022).

We use the same observational data than Yamasaki & Piran (2022), shown in black in Fig. 3. We then fit the data using an MCMC procedure with log-uniform priors such that $1.3 < \log \Gamma < 3.5$; $0 < \log \epsilon_e/\epsilon_B < 4$; $-2 < \log B < 3$; $1 < \log \gamma_m < 7$.

The marginalized posterior distributions for these four parameters are provided on the first row of Fig. 4. As also discussed in Yamasaki & Piran (2022), several spectral solutions are possible. We show for further discussion the posterior distributions of $\hat{\gamma}_m/\gamma_m$, γ_c/γ_m and B/Γ^3 , as well as the distribution of spectral cases in the bottom row of Fig. 4. The best fit model for each of the spectral cases is shown in Fig. 3. We find a high overall agreement with the results of Yamasaki & Piran (2022):

- the identified radiative regimes in the best-fit models are the same: cases F24 and F25 correspond to their cases IIc and III (top row in their Fig. 6), F26 and F27 to their case I (middle row in their Fig. 6), and S11-S14

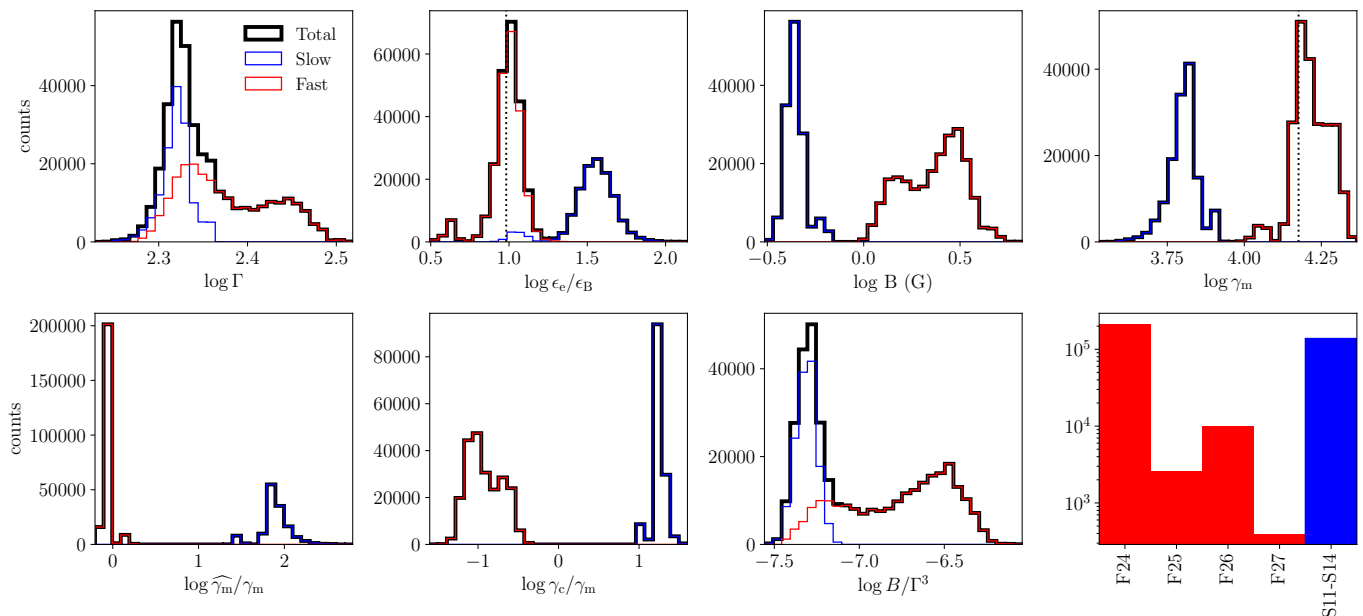


Fig. 4. Marginalized posterior distributions for the spectral fit of the afterglow observations of GRB 190114C at $t_{\text{obs}} = 90$ s. The total (black) is subdivided between the slow (blue) and fast (red) cooling cases. The first row shows the four free parameters explored in this MCMC analysis (Γ , ϵ_e/ϵ_B , B and γ_m). On the second row, we show some derived quantities: $\hat{\gamma}_m/\gamma_m$, γ_c/γ_m and B/Γ^3 . The bottom right panel shows the distribution of the radiative regimes found in the posterior sample (see Appendix B for their description). The best fit model for each radiative regime is shown in Fig. 3.

to one subcase of their slow case I (bottom right panel in their Fig. 6).

- most best models are in fast cooling (see the distribution of γ_c/γ_m in Fig. 4), with electrons at γ_m close to the transition between the Thomson and the KN regimes (see the distribution of $\hat{\gamma}_m/\gamma_m$ in Fig. 4).
- the peak of the posterior distributions of ϵ_e/ϵ_B and γ_m in Fig. 4 are very close to the assumed values in their Fig. 6 (as indicated by the vertical black dotted lines).
- based on the analytical estimates from Derishev & Piran (2021), Yamasaki & Piran (2022) assume a strong correlation between the Lorentz factor and the magnetic field with $B/\Gamma^3 \sim 10^{-7}$. Our MCMC exploration confirms this result but gives an estimate of the dispersion (see the distribution of B/Γ^3 in Fig. 4).

A detailed comparison shows that our results differ slightly on the exact parameter values, owing to some differing normalization constants. It should therefore be kept in mind that the absolute parameter values from spectral fits from different GRB afterglow studies should only be compared if the models used are the same.

The good agreement of our results with Yamasaki & Piran (2022) allows us to validate our radiative model, as both studies are independent implementations of the synchrotron+SSC model using the same level of approximation. In addition, we confirm that this model is a convincing candidate to reproduce the broadband emission of GRB 190114C.

4. The VHE afterglow of GW 170817

Having validated the calculation of the dynamics and synchrotron + SSC emission in our model, we now present the results obtained by fitting the observations of the GRB afterglow of GW 170817, using Bayesian analysis.

4.1. Observational data

In its numerical implementation, our model allows for simultaneous, multi-wavelength modelling. We use 94 data points, from radio to X-rays between 9.2 and 380 days³, as compiled and reprocessed homogeneously by Makhathini et al. (2021). We also include 5 constraining early-time upper limits also reported in Makhathini et al. (2021), as shown in Table 2. Early-time constraints are useful to restrict the posterior models to those with a single peak in flux density, as discussed in § 2.2. All these flux measurements and upper limits are fitted simultaneously.

The likelihood that we use for our study is based on a modified χ^2 calculation to account for the upper limits:

$$\ln \mathcal{L} = -\frac{1}{2} \left[\sum_i \frac{(m_i - d_i)^2}{\sigma_i^2} + \sum_j \frac{(\max\{u_j; m_j\} - u_j)^2}{\sigma_j^2} \right], \quad (80)$$

where the first sum concerns observational data (subscripts i) while the second sum concerns upper limits (subscripts j). The quantities m_i and m_j are the model flux densities at each observing time and frequency of the observational data set; d_i is the flux density value of a detection; σ_i its associated uncertainty; u_j is a flux upper limit presented in Table 2; and σ_j is an equivalent uncertainty that we arbitrarily define as $\sigma_j = 0.2u_j$, which roughly corresponds to the typical uncertainties for the detections. Adding this element accommodates for some models whose predictions are slightly above the reported upper limit. Note that the quantity $\max\{u_j; m_j\}$ in the second term implies

³ Data points are provided by K. Mooley on github.com/kmooley/GW170817/

Table 2. Early-time upper limits used in the afterglow fitting.

Time	Frequency	Instrument	Upper limit
0.57	9.7×10^9	VLA	144
0.70	1.2×10^{18}	NuSTAR	7.3×10^{-4}
1.44	1.0×10^{10}	VLA	13.8
2.40	2.41×10^{17}	Chandra	2.3×10^{-4}
3.35	3×10^9	VLA	19

Notes. Times are given in days, frequencies in Hz, and upper limits in μJy . These flux upper limits are selected as the most constraining among all the early observations listed in the compilation by [Makhathini et al. \(2021\)](#).

that it behaves as a penalty added only for predicted fluxes m_j above the observed upper limits. Another option would be to force the likelihood to diverge as soon as one of the modelled fluxes is above the corresponding upper limit.

In this study, we choose not to include late-time observations after 400 days in the fits. Indeed, we expect jet lateral spreading to play a role at late times, when the shock front reaches Lorentz factors $\Gamma \lesssim 3$, by which point our model cannot accurately describe the jet dynamics. In addition, other emission sites (e.g. the kilonova afterglow, [Nakar & Piran 2011](#)) could also contribute to the observed flux at late times. Including the latest observations ([Hajela et al. 2022](#)) which were not included in the compilation by [Makhathini et al. \(2021\)](#) is also difficult: late-time data in X-rays consists of only a few photons and a correct modelling in this case should be expressed in photon counts and account for the instrumental response and low-statistics effects. The result of such an analysis is currently unclear, with an uncertain late rebrightening ([Hajela et al. 2022](#)): see discussion in [Troja et al. \(2022\)](#). Interpreting the late evolution of GW 170817's afterglow seems to require a dedicated study, and we therefore exclude this phase from the analysis presented here. Finally, we do not include the H.E.S.S. upper limit at the peak ([Abdalla et al. 2020](#)), or the *Fermi*/LAT and H.E.S.S. early upper limits ([Ajello et al. 2018](#); [Abdalla et al. 2017](#)), as it does constrain the fit (see § 4.4).

4.2. Results from the afterglow fitting

We perform a Bayesian analysis on the afterglow data of GW 170817 using the Markov Chain Monte Carlo (MCMC) algorithm of the Python suite `emcee` ([Foreman-Mackey et al. 2013, 2019](#)). We run three separate fits where only the assumptions for the radiative processes in the shocked region differ:

1. "no SSC": emission is only produced by synchrotron radiation, as described in [Sari et al. \(1998\)](#) and § 2.4.4;
2. "SSC (Thomson)": SSC is taken into account assuming that all scatterings occur in Thomson regime, as described in [Sari & Esin \(2001\)](#) and § 2.4.5;
3. "SSC (with KN)": SSC is taken into account including the KN regime, as described in [Nakar et al. \(2009\)](#) and § 2.4.6.

The priors used for these three fits are identical and presented in Table 3. We use (log-)uniform priors over large intervals in order to remain as agnostic as possible. Their bounds are shown in Table 3. Additional constraints on the

Table 3. Free parameters of the MCMC, their prior bounds and shape.

Parameter	Bounds	Type
$E_{0,\text{iso}}^c$ (erg)	$10^{50} - 10^{56}$	log-uniform
θ_c (deg)	0.5 – 10	uniform
θ_v (deg)	0 – 50	uniform
n_{ext} (cm^{-3})	$10^{-6} - 10^0$	log-uniform
ϵ_B	$10^{-6} - 1$	log-uniform
ϵ_e	$10^{-4} - 1$	log-uniform
ζ	$10^{-4} - 1$	log-uniform
p	2.1 – 2.4	uniform
a	0.1 – 7	uniform
Γ_0^c	$10^1 - 10^3$	log-uniform
b	0 – 6	uniform

viewing angle can be obtained by combining the GW signal and the accurate distance and localization of the host galaxy ([Finstad et al. 2018](#)), or by combining the afterglow photometry and VLBI imagery ([Govreen-Segal & Nakar 2023](#)), and the density of the external medium can be constrained from direct observation of the host galaxy ([Hallinan et al. 2017](#); [Hajela et al. 2019](#)). We do not include them to focus on constraints obtained from the afterglow modelling only.

For each of the three fits, we initialize 50 chains and run 10 000 iterations per chain. After studying the convergence speed, we remove the first 2 000 iterations for each chain and show the posterior distributions for the remaining 400 000 samples of parameters.

We present the marginalized posterior distribution of the free parameters for the three fits in Fig. 5, complemented by Fig. B.2 in appendix, which shows the corresponding joint and marginalized posterior distributions at 3σ credibility ("corner plot"). We also show in Fig. 5 the distribution of some derived quantities, the true initial kinetic energy of the ejecta E_0 as deduced from Equation (5), the ratio of the viewing angle over the opening angle of the core jet θ_v/θ_c and the four conditions for single-peaked light curves described by [Beniamini et al. \(2020b\)](#) and in § 2.2. The three fits lead to similar distributions across the pa-

Table 4. Posterior values for the free parameters of the three fits of the afterglow of GW 170817.

Free Parameter	Model		
	no SSC	SSC (Thomson)	SSC (KN)
$\log E_{0,\text{iso}}^c$ [erg]	$53.70^{+1.21}_{-1.15}$	$54.11^{+1.14}_{-1.30}$	$53.70^{+1.12}_{-1.32}$
θ_c [°]	$1.77^{+1.12}_{-0.89}$	$1.85^{+1.28}_{-0.82}$	$2.07^{+0.83}_{-0.82}$
θ_v [°]	$21.81^{+7.69}_{-7.02}$	$17.16^{+2.50}_{-2.35}$	$22.67^{+5.94}_{-5.58}$
$\log n_{\text{ext}}$ [cm^{-3}]	$-1.09^{+1.09}_{-1.28}$	$-1.61^{+1.08}_{-1.23}$	$-1.03^{+1.03}_{-1.14}$
$\log \epsilon_B$	$-4.09^{+1.36}_{-1.01}$	$-4.43^{+1.39}_{-1.54}$	$-4.08^{+1.19}_{-0.97}$
$\log \epsilon_e$	$-2.73^{+0.99}_{-1.27}$	$-2.97^{+1.13}_{-1.03}$	$-2.81^{+1.15}_{-1.13}$
$\log \zeta$	$-0.68^{+0.68}_{-1.05}$	$-0.96^{+0.96}_{-0.96}$	$-0.81^{+0.81}_{-1.07}$
p	$2.14^{+0.02}_{-0.02}$	$2.14^{+0.01}_{-0.01}$	$2.14^{+0.01}_{-0.02}$
a	$3.14^{+0.30}_{-0.29}$	$3.34^{+0.66}_{-0.50}$	$3.19^{+0.30}_{-0.27}$
$\log \Gamma_0^c$	$2.68^{+0.32}_{-0.53}$	$2.62^{+0.38}_{-0.49}$	$2.64^{+0.36}_{-0.51}$
b	$2.13^{+0.84}_{-0.78}$	$2.20^{+1.07}_{-0.97}$	$2.24^{+0.79}_{-0.80}$

Notes. The three fits are presented in § 4.2. The table reports the median value of each parameter's posterior distribution, with uncertainties corresponding to the 90% credible intervals.

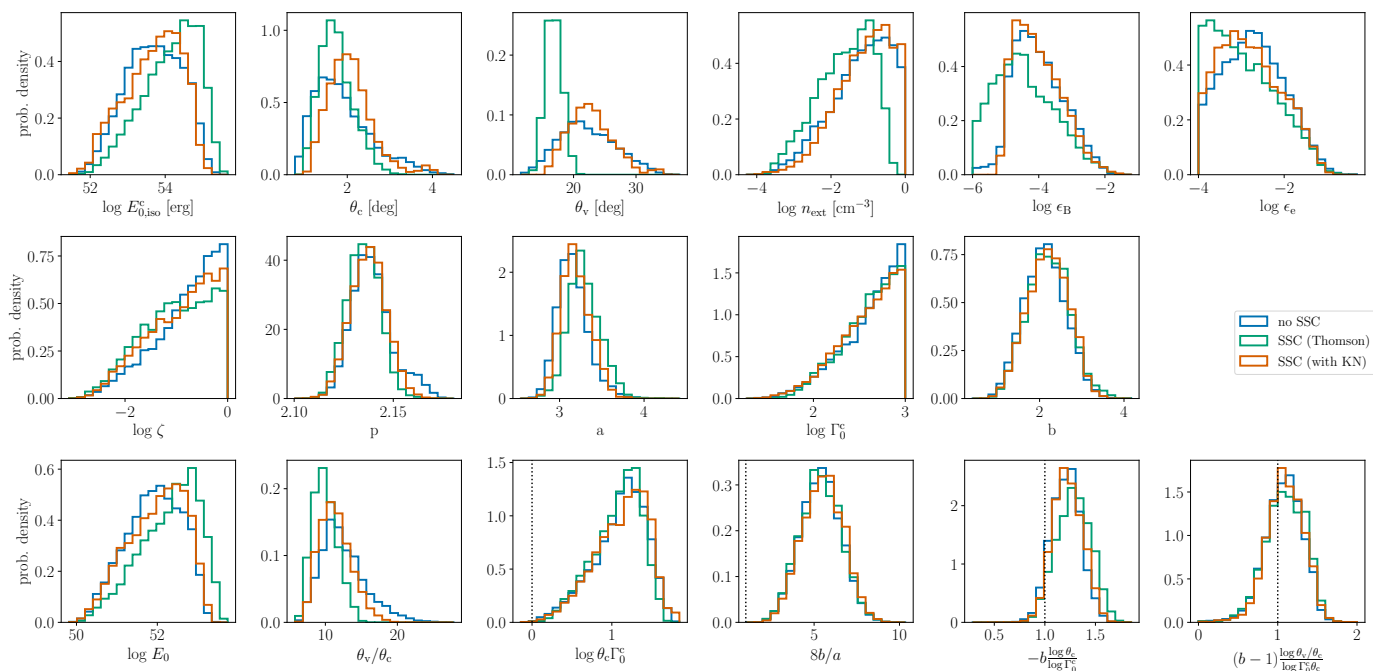


Fig. 5. Comparison of the marginalized posterior distributions for the three fits of the afterglow of GW 170817 presented in Section 4, which differ only by the treatment of the radiative processes: "no SSC" in blue; "SSC (Thomson)" in green; "SSC (with KN)" in orange. The first two rows show the inferred distributions of the model's free parameters. The last row shows the distributions of several quantities derived from these parameters: true energy of the jet E_0 (see Equation (5)), ratio θ_v/θ_c , and four quantities used in the conditions for single-peaked light curves from Beniamini et al. (2020b) and described in § 2.2, $\log(\theta_c\Gamma_0^c)$, $8b/a$, $-b\frac{\log\theta_c}{\log\Gamma_0^c}$ and $(b-1)\frac{\log(\theta_v/\theta_c)}{\log(\Gamma_0^c\theta_c)}$.

parameter space, with a few exceptions discussed in § 4.3. The median parameter values as well as their 90% credible intervals are reported in Table 4. We finally show in Table 5 the median values of the derived quantities shown in Fig. 5.

The detailed joint posterior distributions for the "SSC (with KN)" model where emission is produced by synchrotron radiation and SSC diffusions in both Thomson and KN regimes are shown in Fig. 6. In this figure, which is representative of the results obtained with the three fits, we observe typical correlations between some of the afterglow parameters, like θ_c and θ_v , $E_{0,\text{iso}}^c$ and n_{ext} , or ϵ_e and ϵ_B . Some other parameters are anti-correlated, like $E_{0,\text{iso}}^c$ and ϵ_B , or n_{ext} and ϵ_B . Such degeneracies in the model

Table 5. Posterior values for several derived quantities from the three fits of the afterglow of GW 170817.

Derived quantity	Model		
	no SSC	SSC (Thomson)	SSC (KN)
$\log E_0$ [erg]	$51.95^{+1.05}_{-1.13}$	$52.41^{+1.04}_{-1.22}$	$52.07^{+1.01}_{-1.19}$
θ_v/θ_c	$11.95^{+5.29}_{-4.54}$	$9.84^{+2.80}_{-2.59}$	$11.19^{+3.58}_{-3.45}$
$\log(E_{0,\text{iso}}^c/n_{\text{ext}})$ [erg · cm ³]	$54.90^{+1.08}_{-1.18}$	$55.77^{+0.42}_{-0.43}$	$54.79^{+0.86}_{-0.85}$
$\log(\theta_c\Gamma_0^c)$	$1.15^{+0.48}_{-0.58}$	$1.12^{+0.43}_{-0.54}$	$1.17^{+0.44}_{-0.61}$
$8b/a$	$5.40^{+1.81}_{-2.05}$	$5.36^{+1.95}_{-1.94}$	$5.54^{+1.91}_{-1.96}$
$-b\log\theta_c/\log\Gamma_0^c$	$1.21^{+0.23}_{-0.25}$	$1.29^{+0.27}_{-0.28}$	$1.22^{+0.25}_{-0.22}$
$(b-1)\log(\theta_v/\theta_c)/\log(\Gamma_0^c\theta_c)$	$1.09^{+0.38}_{-0.38}$	$1.10^{+0.39}_{-0.39}$	$1.10^{+0.40}_{-0.34}$

Notes. The three fits are presented in § 4.2 and the posterior values of the free parameters are reported in Table 4. The table reports the median value of each quantity's posterior distribution, with uncertainties corresponding to the 90% credible intervals. The four last rows correspond to the quantities appearing in the conditions for single peak light curves (§ 2.2).

parameters are expected when only the synchrotron component is observed (see e.g. Aksulu et al. 2022). In the case of GW 170817, the afterglow light curves can in first approximation be described by five quantities – its peak time, peak flux, rising and decreasing phase temporal slopes and spectral slope – which does not allow to constrain all the free parameters listed in Table 3.

As a post-processing step, we re-sample 20 000 light curves at several observing frequencies (3 GHz, 1 keV and 1 TeV) and spectra at several observing times (20 days, 110 days, 400 days), where the set of parameters is directly drawn from the posterior sample, for each of the three fits. At each observing time (for the light curves) or at each frequency (for the spectra), we then determine the 68% and 97.5% credible intervals for the distribution of predicted flux densities, that we use to draw confidence contours around the median value of the light curves and spectra. Because the posterior samples are similar between the three models, we show only the results for the most realistic case ("SSC (with KN)" model) in Figs. 7 and 8 (radio and VHE light curve), and in Fig. 9 (spectrum at 110 days, close to the peak).

4.3. Discussion: inferred parameters

As seen in Fig. 7, the afterglow of GW 170817 is very well fitted by the model. The model predicts accurately the flux at all times, with a very small dispersion. The dispersion of the predicted flux is of course larger at very early or very late times where we do not include any data point in the fit. The same quality of the model prediction is observed in

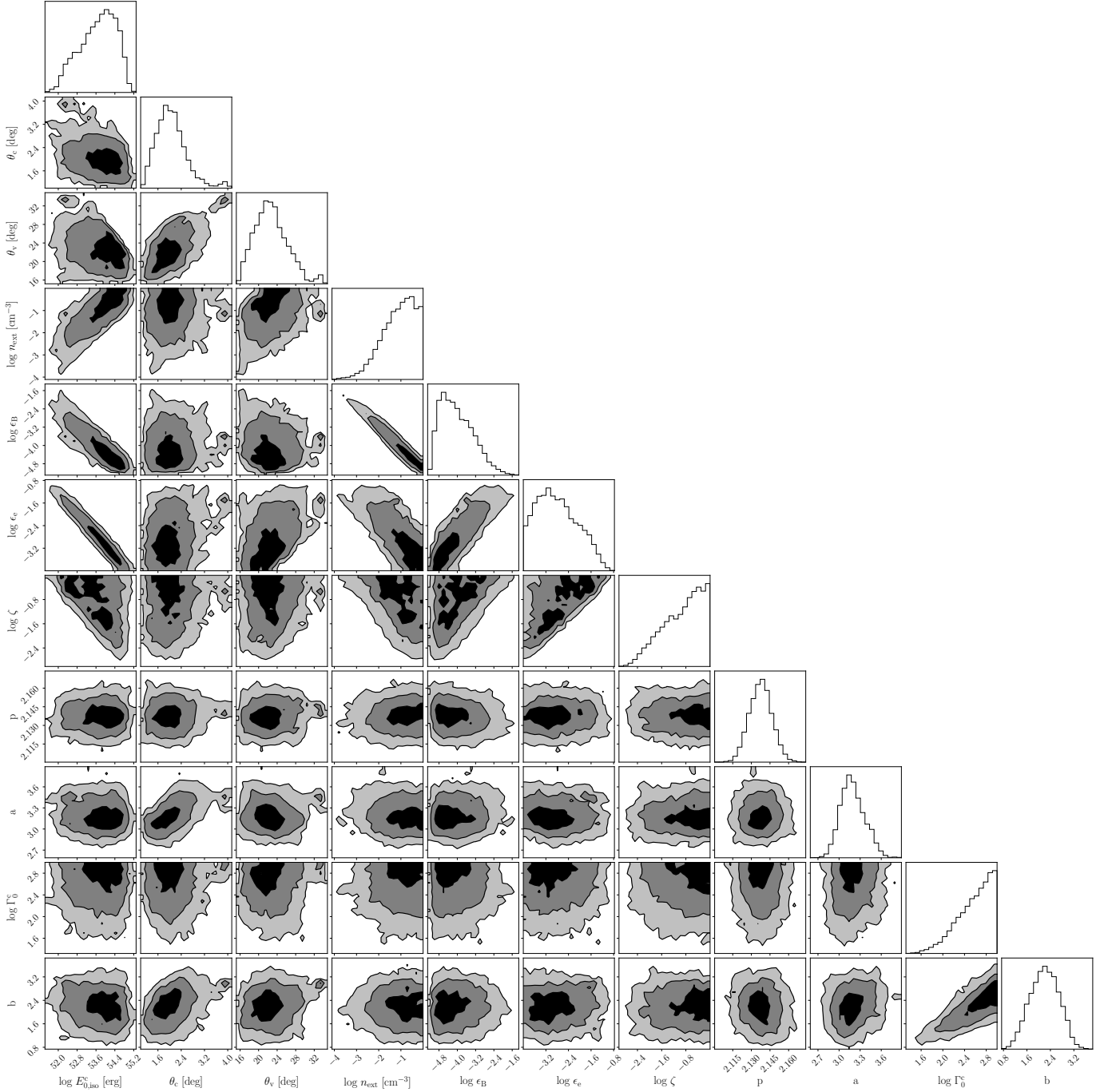


Fig. 6. Posterior joint and marginalized distributions of the model's free parameters, $E_{0,\text{iso}}^C$, θ_c , θ_v , n_{ext} , ϵ_B , ϵ_e , ζ , p , a , Γ_0^C , b , for the "SSC (with KN)" fit of the afterglow of GW 170817 presented in Section 4 which includes SSC diffusions in both Thomson and KN regimes. The priors are all uniform or log-uniform and are shown in Table 3. Fitted data includes all points until $t_{\text{max}} = 400$ days, as well as 5 early-time upper limits (see Section 4.1). The colored contours correspond to the 1σ , 2σ and 3σ confidence intervals for each parameter.

the spectrum on Fig. 9. The frequency $\nu_{\text{m,obs}}$ is below the data points at the lowest frequency, with some dispersion in absence of observational constraints. The critical frequency $\nu_{\text{c,obs}}$ is found to be in X-rays, just above the highest frequency data points.

The inferred values of most model parameters (Fig. 5 and Table 4) are very similar to the results obtained in previous studies modelling the same afterglow with the synchrotron radiation from a decelerating structured jet (Troja

et al. 2019; Lamb et al. 2019; Ghirlanda et al. 2019; Ryan et al. 2020), with some exceptions, due to different priors. A first difference concerns the viewing and core jet opening angles θ_v and θ_c . Even if the values inferred by the "SSC (with KN)" fit are comparable with values found in previous studies, the corresponding ratio $\theta_v/\theta_c \sim 11$ (Table 5) is on the higher end of the other predictions. Nakar & Piran (2021) give a compilation of these predictions and show that afterglow light curves can only constrain this

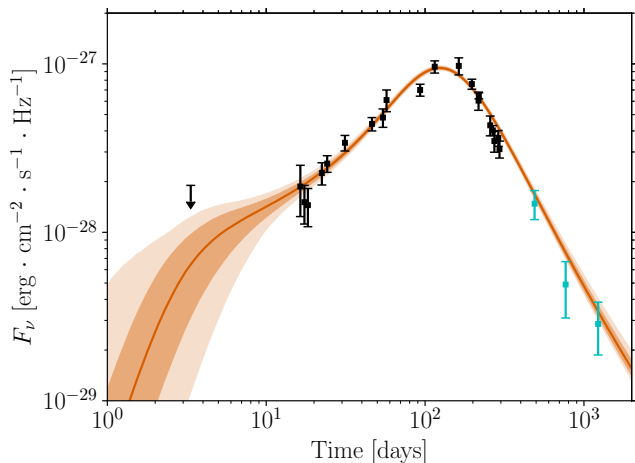


Fig. 7. Posterior distribution of the radio light curves at $\nu_{\text{obs}} = 3$ GHz for the "SSC (with KN)" fit of the afterglow of GW 170817. Solid lines represent the median value at each observing time, dark contours the 68% confidence interval and light contours the 97.5% confidence interval. Late-time observations not used in the fit are shown in blue.

ratio and not the two parameters independently, which is confirmed by the correlation observed in Fig. 6. This difference is probably due to the flat and broad priors we use for these two parameters, whereas most previous studies use much stricter priors based on an external constraint, either on the viewing angle derived from GW data using the value of the Hubble constant from Planck (as in Troja et al. 2019; Ryan et al. 2020) or a constraint on the viewing angle and the core jet using VLBI imagery (as in Ghirlanda et al. 2019; Lamb et al. 2019). The marginalized distributions of θ_v and θ_c show that a restricted region of the parameter space has been explored by the MCMC chains for these parameters, as is also visible on Fig. B.2.

When comparing with the results of Ryan et al. (2020), where the assumptions are the closest to those of our "no SSC" fit and where the light curves are computed using `afterglowpy` with which we compared our model in Section 3, we also find that our predicted values for $E_{0,\text{iso}}^c$ and n_{ext} are about one order of magnitude higher. From Fig. 6, it appears that it is also an effect of our different priors for the angles. However we observe the expected strong correlation between these two parameters and the inferred ratio $E_{0,\text{iso}}^c/n_{\text{ext}} \sim 10^{55} \text{ erg} \cdot \text{cm}^{-3}$ (Table 5) is close to the value obtained by Ryan et al. (2020). Using similar priors for the angles, or including a constraint on the external density from the observation of the host galaxy (Hallinan et al. 2017; Hajela et al. 2019) would then reduce the inferred values for these two parameters. We discuss below the fact that detections in the VHE range would help to break this degeneracy and allow for a more precise determination of the energy and external density independently of such external constraints.

The inferred values for the microphysics parameters ϵ_B and p are very close to those obtained in previous studies. The value of ϵ_e is slightly lower, but we also find that the median value for the fraction of accelerated electrons is ~ 0.15 , whereas this parameter is not included in past studies. Both parameters are strongly correlated, as seen in Fig. 6. Overall, the values of these microphysics param-

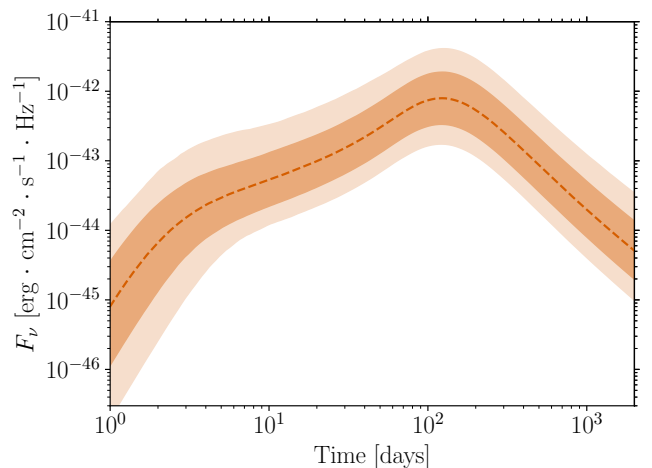


Fig. 8. Posterior distribution of the VHE light curves at $h\nu_{\text{obs}} = 1$ TeV for the "SSC (with KN)" fit of the afterglow of GW 170817. Same conventions as in Fig. 7. Note that this is a prediction of the model, with no observational constraint included in the fit.

eters, including ζ , are in a good agreement with the current understanding of the plasma physics at work in relativistic collisionless shocks (see e.g. Sironi et al. 2015) and comparable to values obtained for cosmological short GRBs by Fong et al. (2015). The inferred value $\zeta < 1$ leads to the question of a possible contribution to the radiation of the remaining thermal electrons (see e.g. Warren et al. 2022). Assuming $\zeta = 1$ as in previous studies is relevant in the case of GW 170817 as the observed emission is dominated by the synchrotron radiation, and the cooling break $\nu_{c,\text{obs}}$ is not detected. However these microphysics parameter impact the synchrotron and SSC components in different manners, as discussed below, and must therefore be considered to predict the VHE emission.

As shown in the second row of Fig. 5 and in Table 5, the inferred values of the parameters describing the initial lateral structure of the ejecta are in good agreement with the conditions established in Beniamini et al. (2020b) and listed in § 2.2 to get a single-peak light curve: note that in practice, double-peak light curves are not excluded a priori in our MCMC, but are disfavored due to the inclusion of early upper limits (Table 2). Finally, we note that the initial distribution of the Lorentz factor (Γ_0^c and b) is not well constrained, which was expected as most of the observed emission is produced in the self-similar stage of the deceleration. A correlation is observed between Γ_0^c and b . This can be explained by the fact that the lateral structure is required to reproduce the early-time slow rise of the light curve (Nakar & Piran 2018). Specifically, some material needs to have lower initial Lorentz factors to overcome effects of Doppler boosting out of the line of sight. With a higher core Γ_0^c , a steeper decrease in $\Gamma_0(\theta)$ is required for material at a given latitude θ to have a sufficiently low initial Lorentz factor that the observed slow rise can be reproduced, leading to higher values of b .

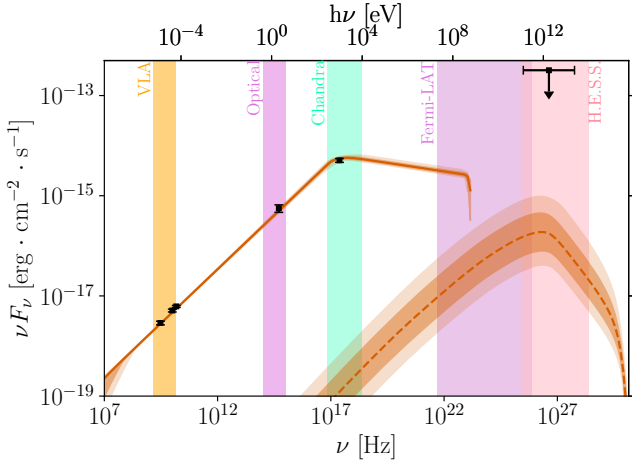


Fig. 9. Posterior distribution of the afterglow spectrum around its peak ($t_{\text{obs}} = 110$ days) for the "SSC (with KN)" fit of the afterglow of GW 170817. Data points show the multi-wavelength observations at $t_{\text{obs}} \pm 4$ days. The upper limit from H.E.S.S. is also indicated (Abdalla et al. 2020). The low-energy component (solid line) is produced by synchrotron radiation, while the high-energy emission (dashed line) is powered by SSC diffusions. Thick lines represent the median value at each observing frequency, dark contours the 68% confidence interval and light contours the 97.5% confidence interval. Some instrument observing spectral ranges are shown in colors.

4.4. Discussion: the predicted VHE emission of GW 170817

We now discuss the predicted VHE emission of the afterglow of GW 170817. The predicted light curve at 1 TeV is plotted in Fig. 8 and the VHE component of the spectrum at the peak of the light curve is shown in Fig. 9, where is also indicated the upper limit obtained by H.E.S.S. (Abdalla et al. 2020). It appears that (i) the synchrotron emission extends at most up to the GeV range⁴ (due to the synchrotron burnoff limit, see Appendix A) and the VHE emission is then entirely due to the SSC process; (ii) even taking into account the dispersion, the predicted flux at 1 TeV is at least two orders of magnitude below the upper limit of $3.2 \times 10^{-13} \text{ erg} \cdot \text{s}^{-1} \cdot \text{cm}^{-2}$ obtained around the peak by H.E.S.S. (Abdalla et al. 2020), which is therefore not constraining. It is also clear when comparing Figs. 7 and 8 that the dispersion of the predicted VHE flux is much larger than for the synchrotron component which is well constrained by the observations from radio to X-rays. This is also shown in the distribution of the predicted peak flux and peak time in radio and at 1 TeV in Fig. 10. Note that the VHE light curve peaks a few days before the light curves from radio to X-rays, due to a different evolution of the synchrotron and SSC components. This result is due to the fact that the dependency of the SSC component on the model parameters is complex and very different from the dependencies of the synchrotron component identified by Sari et al. (1998). This also highlights the interest of detecting the VHE emission for the inference of model pa-

⁴ The emission in the 0.1 – 1 GeV range is then dominated by the synchrotron radiation. For comparison with Fig. 9, the sensitivity of *Fermi*/LAT above 100 MeV is of the order of $10^{-11} \text{ erg} \cdot \text{s}^{-1} \cdot \text{cm}^{-2}$ for a ~ 1 day observation (Abdollahi et al. 2020, 2022). The afterglow of GW 170817 was therefore undetectable by *Fermi*/LAT at any time.

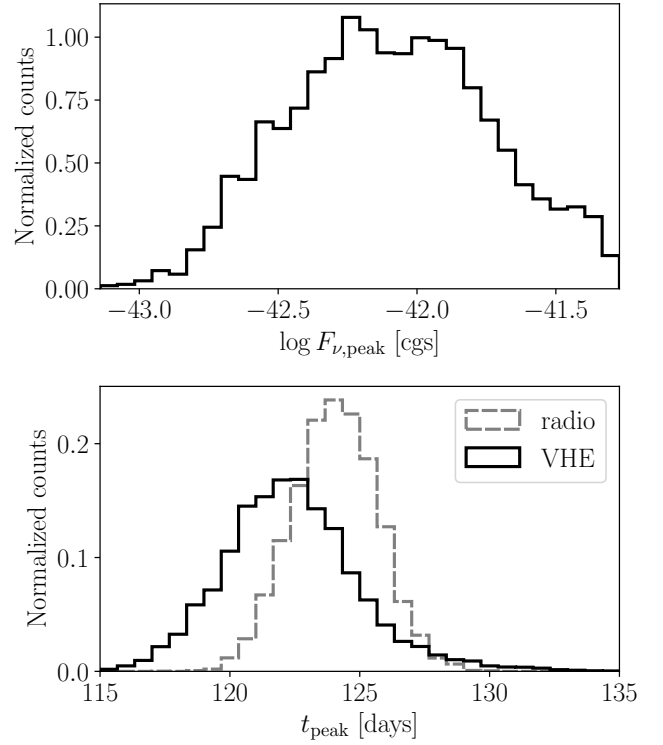


Fig. 10. Posterior distributions of the VHE peak flux density (top) and the radio (dashed grey line) and VHE (solid black line) peak times (bottom) for the "SSC (with KN)" fit of the afterglow of GW 170817.

rameters, as some of the degeneracies visible in Fig. 6 would be broken.

In the afterglow of GW 170817, the synchrotron spectrum is in slow cooling, with a spectral peak determined by the critical Lorentz factor γ_c . If IC scatterings occurred in Thomson regime, the peak of the SSC component would be due to the diffusion of photons at ν_c by the electrons at γ_c (Sari & Esin 2001), and this peak should be intense as $\epsilon_e \gg \epsilon_B$ (see Equation (60)). However, the predicted VHE emission is actually very weak because of a strong KN attenuation. To illustrate this effect, we select in Table 6 two reference sets of parameters, taken from the posterior sample. They are respectively in the 68% and 97.5% confidence intervals for the "SSC (with KN)" fit and fit perfectly well the observed light curves. The first set of parameters ("Moderate") corresponds to a predicted VHE flux which is close to the median, whereas the second set of parameters ("Optimistic") corresponds to a predicted VHE flux on the highest end of the confidence interval: see the two predicted VHE light curves and peak spectra in Fig. 11. In both cases, we selected sets of parameters having a low density, and therefore a low energy (see discussion in § 4.3).

Fig. 12 shows for these two reference cases the evolution of $Y(\gamma_c)$ and $\gamma_c/\hat{\gamma}_c$ for the core jet, computing the SSC emission either by assuming that all scatterings are in Thomson regime like in the "SSC (Thomson)" fit, or by including the KN attenuation like in the "SSC (with KN)" fit. The figure shows that, in the full calculation, $\gamma_c/\hat{\gamma}_c \gg 1$ during the whole evolution, so that the scatterings of photons at ν_c by electrons at γ_c are strongly reduced by the KN regime. The Compton parameter $Y(\gamma_c)$ then remains very low. This

Table 6. Parameters of the two reference cases.

Parameter	"Moderate"	"Optimistic"
$E_{0,\text{iso}}^c$ [erg]	4.12×10^{52}	5.07×10^{52}
θ_c [°]	1.75	1.31
θ_v [°]	21.25	24.40
n_{ext} [cm ⁻³]	4.25×10^{-3}	1.52×10^{-2}
ϵ_B	1.61×10^{-3}	4.79×10^{-4}
ϵ_e	1.87×10^{-2}	3.54×10^{-2}
ζ	1	3.57×10^{-1}
p	2.139	2.149
a	2.98	2.95
Γ_0^c	184	164
b	2.01	1.34

Notes. Both sets of parameters are in the 97.5% confidence interval of the distributions inferred by the "SSC (with KN)" fit of the afterglow of GW 170817. They differ by the predicted VHE flux, which is either close to the median ("Moderate" case) or at the higher end of the confidence interval ("Optimistic" case).

confirms the origin of the weak VHE emission in the afterglow of GW 170817. In this regime of weak SSC emission, the synchrotron component is unaffected by the IC cooling, $\gamma_c \simeq \gamma_c^{\text{syn}}$, and this explains why the results of the "no SSC" and "SSC (with KN)" fits are so close (Table 4). On the other hand, Fig. 12 also shows that $Y^{\text{no KN}}$ overestimates $Y(\gamma_c)$ in this case, leading to $Y(\gamma_c) > 1$. The critical Lorentz factor is therefore given by $\gamma_c \simeq \gamma_c^{\text{syn}}/Y(\gamma_c)$, which leads to an overestimation of γ_c^{syn} in the MCMC to maintain the cooling break above the X-ray measurements (increased $E_{0,\text{iso}}$ and lower ϵ_B). This explains the observed difference between the values of the model parameters inferred in the "SSC (Thomson)" and "SSC (with KN)" fits in Table 4. The value of $\gamma_c/\hat{\gamma}_c \gg 1$ in this case (green curves in the top panel of Fig. 12) proves that the Thomson regime is not justified.

As the upper limit of H.E.S.S. was obtained close to the predicted peak with an already long exposure time of 53.9 hours (Abdalla et al. 2020), our prediction shows that it was unfortunately impossible to detect the VHE afterglow of GW 170817 with instruments currently available. We discuss in the next section the conditions that would make a post-merger afterglow detectable at VHE in the future, especially in the context of the increased sensitivity expected with the CTA.

5. Detectability of post-merger afterglows at VHE and prospects for the CTA

Even if the VHE afterglow of GW 170817 was not detectable, deeper observations of similar events can be expected in the future, in particular with the Cherenkov Telescope Array (CTA, Cherenkov Telescope Array Consortium et al. 2019). The off-axis afterglow phase is of particular interest because after a few days, full-night observations can be conducted without a significant intrinsic source flux variability over the observation time. We investigate in this section the conditions that would make such an event detectable by current instruments and the upcoming CTA. For this study, we assume a CTA detection sensitivity at 1 TeV about 6 times better than that of H.E.S.S., as ex-

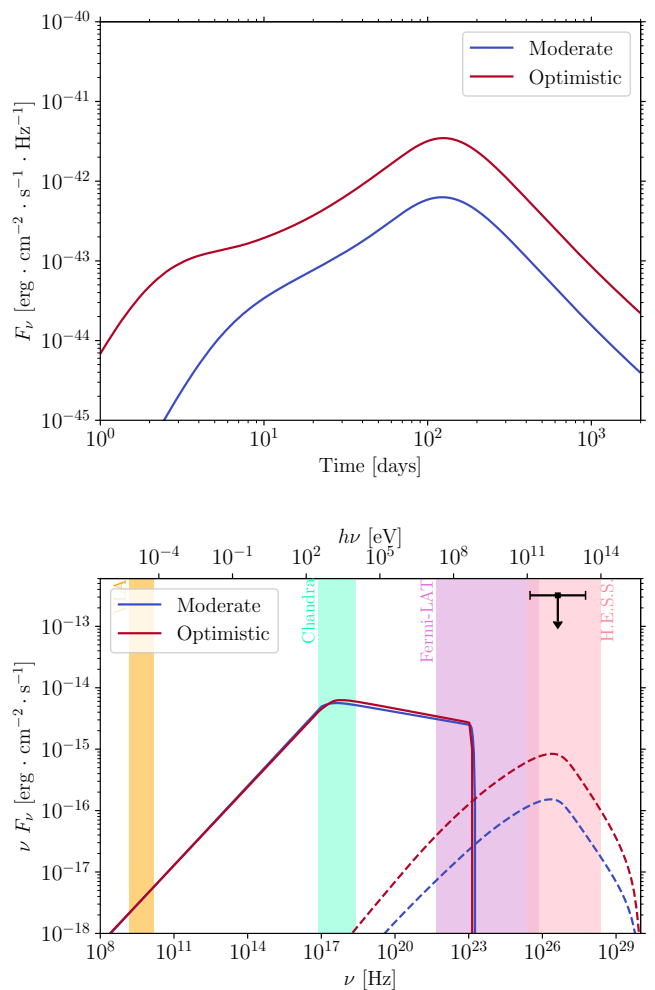


Fig. 11. VHE light curve at $h\nu_{\text{obs}} = 1$ TeV (top) and spectrum around the peak at $t_{\text{obs}} = 110$ days (bottom) for the "Moderate" (in blue) and "Optimistic" (in red) reference cases (see Table 6). Both predict similar fluxes in the synchrotron range due to the observational constraints, but differ in the SSC regime. The upper limit from H.E.S.S. is indicated for comparison (Abdalla et al. 2020).

pected from Cherenkov Telescope Array Consortium et al. (2019). For an exposure time of ~ 50 hours as for the H.E.S.S. deep observations of GW 170817 (Abdalla et al. 2020), this leads to a detection sensitivity at 1 TeV of 5×10^{-14} erg · s⁻¹ · cm⁻².

A geometrical effect such as a lower viewing angle naturally increases the peak of the observed flux, and has a similar effect on the synchrotron and SSC components. In Fig. 13, we show for the "Moderate" reference case the light curves (top) and spectra at the time of the 1 TeV emission peak (bottom), for gradually decreasing viewing angles. The 1 TeV light curves peak at earlier times when the viewing angle decreases, and the peak flux reaches higher values. As expected, the relative flux increase at the time of peak is similar for the synchrotron and the SSC components (Fig. 13, bottom) and all light curves follow a similar long-term evolution, when the entire jet emission becomes visible to the off-axis observer. For the "Moderate" (resp. "Optimistic") reference case (Table 6), we find that a ratio $\theta_v/\theta_c \lesssim 3$ (resp. $\theta_v/\theta_c \lesssim 6$) would have made the afterglow of GW 170817 detectable by H.E.S.S., provided the condi-

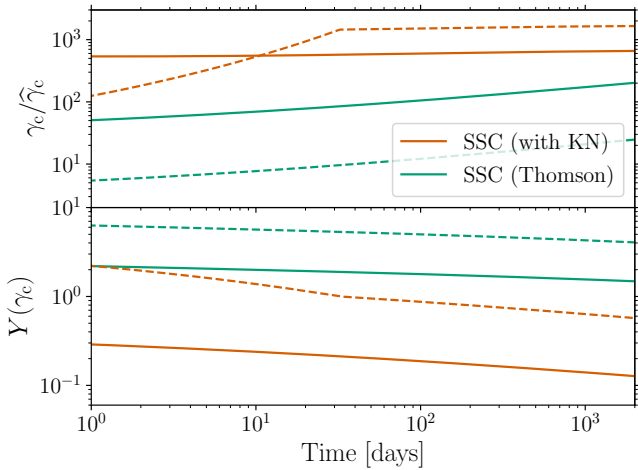


Fig. 12. Evolution of $\gamma_c/\hat{\gamma}_c$ (top) and of the Compton parameter at γ_c , $Y(\gamma_c)$ (bottom) in the core jet. These quantities are plotted as a function of the observer time for the "Moderate" (solid line) and "Optimistic" (dashed line) reference cases (see Table 6) in the "SSC (Thomson)" case (green) and in the "SSC (with KN)" case (orange).

tions had allowed for a very early deep observation. With the CTA, the VHE emission could have been detected up to $\theta_v/\theta_c \simeq 4$ (resp. $\theta_v/\theta_c \simeq 8$). In such a scenario, the emission peaks at ~ 5 days (resp. 13 days). This opens up interesting perspectives, even if the expected detection rate of nearby events at small viewing angles is low (see e.g. Duque et al. 2019; Mochkovitch et al. 2021).

Under some conditions, the predicted VHE emission could also be intrinsically brighter. As discussed in § 4.4, the VHE afterglow of GW 170817 is weak because of a strong KN attenuation ($\gamma_c/\hat{\gamma}_c \gg 1$). The regime for the diffusions of photons at ν_c by electrons at γ_c is affected by several parameters (Nakar 2007). When the diffusions occur in the Thomson regime, the predicted scaling in the core jet is

$$\frac{\gamma_c}{\hat{\gamma}_c} \propto \frac{1}{(1 + Y_c)^3} \frac{1}{\epsilon_B^{5/2} n_{\text{ext}}^{3/2} \epsilon_0^c}. \quad (81)$$

Therefore, the Thomson regime is favored by a high magnetic field, a high density or a high kinetic energy. As ϵ_B is determined by plasma instabilities at the ultra-relativistic shock (Sironi et al. 2015), it should not vary much from an afterglow to another. On the other hand, the external density and the kinetic energy may differ between mergers. We focus here on the effect of the external density, which is slightly stronger. Fig. 14 shows the evolution of the afterglow emission for the "Moderate" reference case when n_{ext} increases up to $\sim 10 \text{ cm}^{-3}$, all other parameters being kept constant. A higher external density leads to an earlier peak time at higher luminosities but affects differently the synchrotron and the SSC flux: as expected the SSC process becomes more efficient and the relative SSC-to-synchrotron ratio increases. The transition from the weak SSC emission due to a strong KN attenuation described in § 4.4 to a more efficient case in Thomson regime occurs in this reference case above $n_{\text{ext}} \sim 1 \text{ cm}^{-3}$. This corresponds to the radiative regime S15 in Appendix B, with spectral breaks at $\nu_m < \nu_c < \hat{\nu}_c < \nu_0$. This effect can clearly be observed on the bottom panel of Fig. 14, showing the observed spectrum

at the peak emission. At the largest external densities, the increase of the VHE flux stalls for two reasons. Firstly, the strong SSC emission starts to affect significantly the synchrotron spectrum, which features two peaks (visible on the bottom panel of Fig. 14). The cooling frequency ν_c at the peak also decreases, shifting the SSC peak to lower frequencies so that the flux at 1 TeV does not increase as significantly as the SSC peak flux. A second limitation, dominant at the highest densities, comes from the pair production.

Even taking into account these limitations, a higher external density clearly favors a brighter VHE emission, even if both the "Moderate" and "Optimistic" reference cases remain undetectable by H.E.S.S. or the CTA at the reference viewing angle. We conclude that post-merger VHE afterglows should become detectable in the future only under several favourable conditions, e.g. a higher external density and a slightly lower viewing angle. For instance, the "Moderate" (resp. "Optimistic") reference case with an external density $n_{\text{ext}} = 1 \text{ cm}^{-3}$ and a viewing angle $\theta_v/\theta_c = 6$ should be detectable by the CTA⁵ up to a distance of ~ 90 Mpc (resp. ~ 400 Mpc). Note however that two additional effects should be included in the "Optimistic" case and may reduce this maximum distance: (i) at 400 Mpc, the attenuation by the extragalactic background light is not negligible anymore at 1 TeV (see e.g. Domínguez et al. 2011); (ii) in this case, the VHE afterglow peaks very early (~ 1 day). This would require an early follow-up which will necessarily be less deep due to a limited exposure time. It remains that detections with the CTA above 100 Mpc are possible in the "Optimistic" case. As some parameters that are naturally degenerate in an afterglow fit including only synchrotron radiation, such as n_{ext} and ϵ_B , have different effects on the SSC emission, such VHE detections would therefore better constrain the parameter space and allow for a better understanding of the physical conditions in the post-merger relativistic ejecta.

Another direct consequence of the impact of n_{ext} on SSC emission is that short GRB afterglows detected at VHE are more likely to originate from mergers occurring in a denser environment. Such VHE detections could therefore be unique probes to high-density media at the location of BNS mergers, which are sought clues for short merger time binaries. Fast mergers are indeed expected to occur close to their formation sites, where the external medium density is expected to be higher (see e.g. the discussion in Duque et al. 2020). Population synthesis studies have shown that the yet poorly-constrained phase of common envelope during binary stellar evolution can lead to the production of BNS with very short initial separations that merge rapidly, as discussed by e.g. Dominik et al. (2012). Favorable kick intensities and orientations during the supernovae could also tend to shrink the initial orbital separation and increase the orbital eccentricity for part of the BNS population (Kalogera 1996). Observationally, the projected offset distribution of BNS mergers in their host galaxy seems to feature a tail below 1 half-light radius for $\sim 20\%$ of systems (Fong & Berger 2013; Berger 2014). These observations suffer from several observational biases like afterglow detection, host galaxy association and projection effects,

⁵ On the other hand, even with $n_{\text{ext}} = 1 \text{ cm}^{-3}$ and $\theta_v/\theta_c = 6$, the emission in the *Fermi*/LAT range at the peak is still dominated by the synchrotron radiation and remains undetectable at 40 Mpc for a ~ 1 day observation.

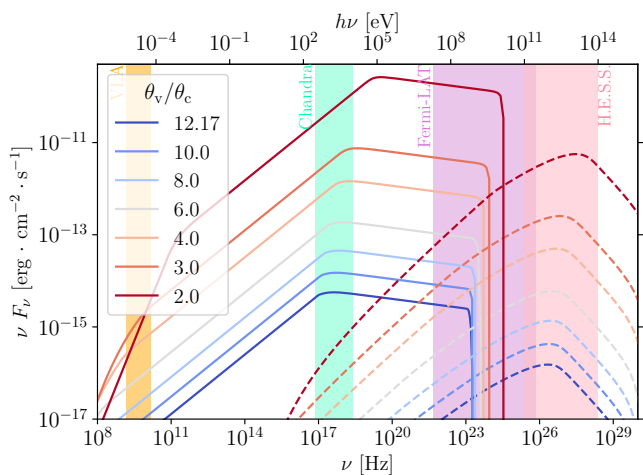
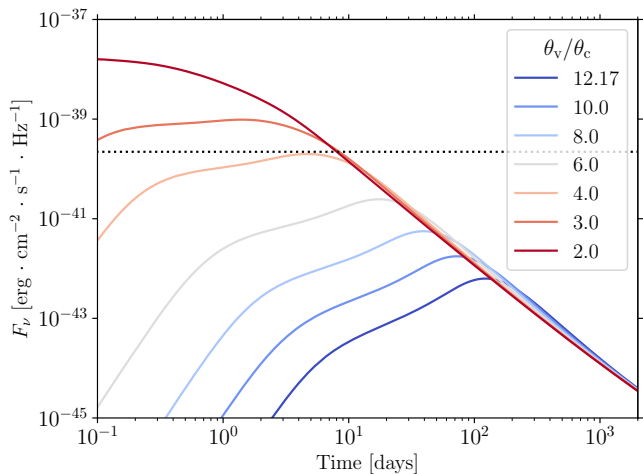


Fig. 13. Light curves at 1 TeV (top panel) and spectra at light curve peak (bottom panel) of the "Moderate" reference case (see Table 6) for varying viewing angles. The case fitting the afterglow of GW 170817 corresponds to $\theta_v/\theta_c = 12.17$. The peak times at which spectra are calculated are (in the ordering of the legend) 123, 73, 39, 17, 4.7, 1.4 and 0.06 days. The dotted line in the top panel corresponds to the assumed CTA sensitivity in Section 5.

probably leading to sample incompleteness, but give evidence for a population of fast mergers. If BNS mergers are the dominant site for r -process nucleosynthesis (see e.g. Lattimer & Schramm 1974; Goriely et al. 2011; Just et al. 2015; Côté et al. 2017), another more indirect evidence is provided by the observed large scatter of [Eu/Fe] abundances in extremely metal-poor stars (see the compilation by Suda et al. 2008), which requires fast mergers allowing the production of r -process elements when the environment is still extremely metal-poor (see e.g. Vangioni et al. 2016; Côté et al. 2019; Dvorkin et al. 2021). It has already been suggested by Duque et al. (2020) that multi-messenger observations of BNS including the detection of the afterglow will be biased in favor of high-density environment, thus allowing to probe this potential population of fast mergers. We show here that future VHE afterglow detections either following the GW detection of a BNS merger, or the detection of a short GRB, can also directly probe this population.

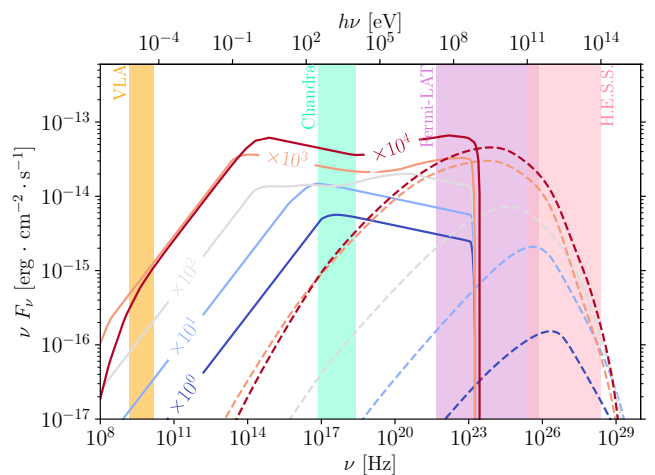
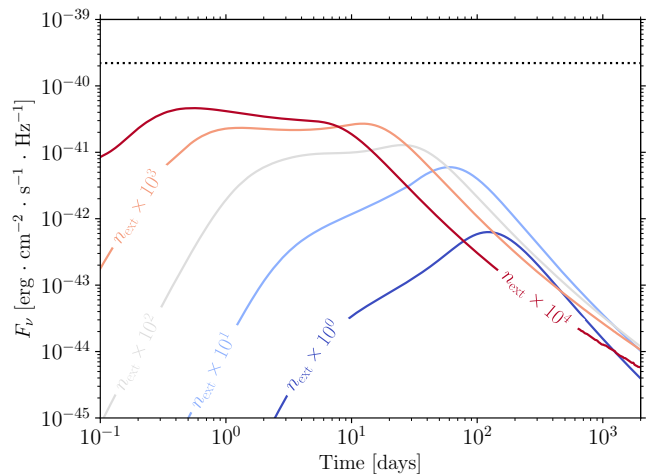


Fig. 14. Light curves at 1 TeV (top panel) and spectra at light curve peak (bottom panel) of the "Moderate" reference case (see Table 6) for varying external medium densities n_{ext} . The case fitting the afterglow of GW 170817 corresponds to $n_{\text{ext}} = 4.25 \times 10^{-3} \text{ cm}^{-3}$. Each line is labeled with the multiplication factor applied to the reference n_{ext} . The peak times at which spectra are calculated are 123, 60, 26, 12 and 0.55 days. The dotted line in the top panel corresponds to the assumed CTA sensitivity in Section 5.

6. Conclusion

We developed a detailed model of the afterglow of a laterally-structured jet from radio to VHE. Emission is produced in the shocked external medium behind the forward external shock and the dynamics does not include the late lateral expansion of the ejecta. Such effects, as well as the contribution of the reverse shock, will be implemented in the future. The main challenge addressed in this paper is the self-consistent calculation of the synchrotron and SSC emission while accounting for the two different IC regimes: Thomson and Klein-Nishina (KN). We based our approach on the method proposed by Nakar et al. (2009), extended to include additional effects: the maximum electron Lorentz factor γ_{max} is also computed self-consistently, leading to a realistic estimate of the high-energy cutoff of the synchrotron component, and the attenuation at high-energy due to pair production is also included. The values of γ_c and $Y(\gamma_c)$, as well as the spectral regimes are determined

numerically. Synchrotron self-absorption, that is relevant at low radio frequencies, has not been included yet. The implementation of the model is computationally-efficient, allowing for afterglow fitting.

We used this model to fit the multi-wavelength afterglow of GW 170817, including radio to X-ray observations up to 400 days and five early-time upper limits. We inferred the model parameters using three different assumptions for the emission: pure synchrotron, synchrotron and SSC assuming that all scatterings occur in Thomson regime, and self-consistent synchrotron and SSC calculation taking into account the KN regime. We obtain excellent fits in the three cases, with similar constraints on the parameters for the pure synchrotron case and the full calculation with SSC in KN regimes, whereas the case where all scatterings are assumed to be in the Thomson regime deviates significantly. The SSC emission in the afterglow of GW 170817 is indeed weak due to a strong KN attenuation, which confirms the need to include the self-consistent calculation of the SSC emission in the KN regime in afterglow models. The predicted VHE flux at the peak has a large dispersion but remains about two orders of magnitude below the upper limit obtained around the peak by H.E.S.S. This shows that the VHE afterglow of GW 170817 was undetectable by current instruments, but that future detections of similar events would break some degeneracies among the model parameters and allow better constraints on the physics of the relativistic ejecta.

We then studied how such post-merger VHE afterglows may become detectable in the future, in the context of the improved sensitivity of the CTA. Beyond the evident effect of a less off-axis viewing angle, we show that the efficiency of the SSC emission becomes larger in external media with higher densities than GW 170817. For instance, a similar ultra-relativistic jet in a medium of density $\sim 1 \text{ cm}^{-3}$ and seen slightly less off-axis than GW 170817 may become detectable by the CTA at 100-400 Mpc.

This bias of VHE afterglow detections in favor of high-density environments offers a new probe of a possible population of fast mergers. With a short merger time, a merger should indeed occur in more central, and denser, regions of its host galaxy. Thus, future detections of such VHE afterglows would not only advance our physical understanding of relativistic jets produced after a BNS merger, but also constrain the physics of the evolution of massive binary systems.

Acknowledgements

Clément Pellouin acknowledges funding support from the Initiative Physique des Infinis (IPI), a research training program of the Idex SUPER at Sorbonne University. The authors acknowledge the Centre National d'Études Spatiales (CNES) for financial support in this research project. This work made use of the Infinity computing cluster at IAP. The authors thank K. Mooley for providing GW 170817 afterglow observation data at github.com/kmooley/GW170817/. This work made use of Python 3.8 and of the Python packages `arviz` (Kumar et al. 2019), `astropy` (Astropy Collaboration et al. 2022), `corner` (Foreman-Mackey 2016), `emcee` (Foreman-Mackey et al. 2019, 2013), `matplotlib` (Hunter 2007), `multiprocessing`, `numpy` (Harris et al. 2020), `pandas` (McKinney 2010), `scipy` (Virtanen et al. 2020).

References

- Abbott, B. P., Abbott, R., Abbott, T. D., et al. 2017a, *Phys. Rev. Lett.*, **119**, 161101
- Abbott, B. P., Abbott, R., Abbott, T. D., et al. 2017b, *ApJ*, **848**, L12
- Abdalla, H., Abramowski, A., Aharonian, F., et al. 2017, *ApJ*, **850**, L22
- Abdalla, H., Adam, R., Aharonian, F., et al. 2020, *ApJ*, **894**, L16
- Abdalla, H., Adam, R., Aharonian, F., et al. 2019, *Nature*, **575**, 464
- Abdollahi, S., Acero, F., Ackermann, M., et al. 2020, *ApJS*, **247**, 33
- Abdollahi, S., Acero, F., Baldini, L., et al. 2022, *ApJS*, **260**, 53
- Acciari, V. A., Ansoldi, S., Antonelli, L. A., et al. 2021, *ApJ*, **908**, 90
- Ajello, M., Allafort, A., Axelsson, M., et al. 2018, *ApJ*, **861**, 85
- Aksulu, M. D., Wijers, R. A. M. J., van Eerten, H. J., & van der Horst, A. J. 2022, *MNRAS*, **511**, 2848
- Ascenzi, S., Oganessian, G., Salafia, O. S., et al. 2020, *A&A*, **641**, A61
- Astropy Collaboration, Price-Whelan, A. M., Lim, P. L., et al. 2022, *ApJ*, **935**, 167
- Balasubramanian, A., Corsi, A., Mooley, K. P., et al. 2021, *ApJ*, **914**, L20
- Beniamini, P., Duque, R., Daigne, F., & Mochkovitch, R. 2020a, *MNRAS*, **492**, 2847
- Beniamini, P., Granot, J., & Gill, R. 2020b, *MNRAS*, **493**, 3521
- Beniamini, P., Nava, L., Duran, R. B., & Piran, T. 2015, *MNRAS*, **454**, 1073
- Berger, E. 2014, *ARA&A*, **52**, 43
- Blanch, O., Longo, F., Berti, A., et al. 2020, GRB Coordinates Network, **29075**, 1
- Blandford, R. D. & McKee, C. F. 1976, *Physics of Fluids*, **19**, 1130
- Bošnjak, Z., Daigne, F., & Dubus, G. 2009, *A&A*, **498**, 677
- Bromberg, O., Nakar, E., Piran, T., & Sari, R. 2011, *ApJ*, **740**, 100
- Bromberg, O., Tchekhovskoy, A., Gottlieb, O., Nakar, E., & Piran, T. 2018, *MNRAS*, **475**, 2971
- Cantiello, M., Jensen, J. B., Blakeslee, J. P., et al. 2018, *ApJ*, **854**, L31
- Cherenkov Telescope Array Consortium, Acharya, B. S., Agudo, I., et al. 2019, Science with the Cherenkov Telescope Array (World Scientific)
- Côté, B., Belczynski, K., Fryer, C. L., et al. 2017, *ApJ*, **836**, 230
- Côté, B., Eichler, M., Arcones, A., et al. 2019, *ApJ*, **875**, 106
- Cowperthwaite, P. S., Berger, E., Villar, V. A., et al. 2017, *ApJ*, **848**, L17
- Daigne, F. & Mochkovitch, R. 1998, *MNRAS*, **296**, 275
- Daigne, F. & Mochkovitch, R. 2000, *A&A*, **358**, 1157
- D'Avanzo, P., Campana, S., Salafia, O. S., et al. 2018, *A&A*, **613**, L1
- Derishev, E. & Piran, T. 2021, *ApJ*, **923**, 135
- Derishev, E. & Piran, T. 2024, *MNRAS*, **530**, 347
- Derishev, E. V., Kocharovsky, V. V., & Kocharovsky, V. V. 2001, *A&A*, **372**, 1071
- Domínguez, A., Primack, J. R., Rosario, D. J., et al. 2011, *MNRAS*, **410**, 2556
- Dominik, M., Belczynski, K., Fryer, C., et al. 2012, *ApJ*, **759**, 52
- Duffell, P. C. & Laskar, T. 2018, *ApJ*, **865**, 94
- Duque, R., Beniamini, P., Daigne, F., & Mochkovitch, R. 2020, *A&A*, **639**, A15
- Duque, R., Beniamini, P., Daigne, F., & Mochkovitch, R. 2022, *MNRAS*, **513**, 951
- Duque, R., Daigne, F., & Mochkovitch, R. 2019, *A&A*, **631**, A39
- Dvorkin, I., Daigne, F., Goriely, S., Vangioni, E., & Silk, J. 2021, *MNRAS*, **506**, 4374
- Finstad, D., De, S., Brown, D. A., Berger, E., & Biwer, C. M. 2018, *ApJ*, **860**, L2
- Fong, W. & Berger, E. 2013, *ApJ*, **776**, 18
- Fong, W., Berger, E., Margutti, R., & Zauderer, B. A. 2015, *ApJ*, **815**, 102
- Foreman-Mackey, D. 2016, *The Journal of Open Source Software*, **1**, 24
- Foreman-Mackey, D., Farr, W., Sinha, M., et al. 2019, *The Journal of Open Source Software*, **4**, 1864
- Foreman-Mackey, D., Hogg, D. W., Lang, D., & Goodman, J. 2013, *PASP*, **125**, 306
- Galván, A., Fraija, N., & González, M. M. 2019, in International Cosmic Ray Conference, Vol. 36, 36th International Cosmic Ray Conference (ICRC2019), 681
- Genet, F., Daigne, F., & Mochkovitch, R. 2007, *MNRAS*, **381**, 732
- Ghirlanda, G., Salafia, O. S., Paragi, Z., et al. 2019, *Science*, **363**, 968
- Gill, R. & Granot, J. 2018, *MNRAS*, **478**, 4128
- Gill, R. & Granot, J. 2022, *Galaxies*, **10**, 74
- Gill, R. & Granot, J. 2023, *MNRAS*, **524**, L78
- Goldstein, A., Veres, P., Burns, E., et al. 2017, *ApJ*, **848**, L14

- Goriely, S., Bauswein, A., & Janka, H.-T. 2011, *ApJ*, **738**, L32
- Gottlieb, O., Nakar, E., Piran, T., & Hotokezaka, K. 2018, *MNRAS*, **479**, 588
- Govreen-Segal, T. & Nakar, E. 2023, *MNRAS*, **524**, 403
- Granot, J. & Piran, T. 2012, *MNRAS*, **421**, 570
- Granot, J., Piran, T., & Sari, R. 1999, *ApJ*, **513**, 679
- H. E. S. S. Collaboration, Abdalla, H., Aharonian, F., et al. 2021, *Science*, **372**, 1081
- Hajela, A., Margutti, R., Alexander, K. D., et al. 2019, *ApJ*, **886**, L17
- Hajela, A., Margutti, R., Bright, J. S., et al. 2022, *ApJ*, **927**, L17
- Hallinan, G., Corsi, A., Mooley, K. P., et al. 2017, *Science*, **358**, 1579
- Harris, C. R., Millman, K. J., van der Walt, S. J., et al. 2020, *Nature*, **585**, 357
- Hunter, J. D. 2007, *Computing in Science and Engineering*, **9**, 90
- Jacovich, T. E., Beniamini, P., & van der Horst, A. J. 2021, *MNRAS*, **504**, 528
- Just, O., Bauswein, A., Ardevol Pulpillo, R., Goriely, S., & Janka, H. T. 2015, *MNRAS*, **448**, 541
- Kalogera, V. 1996, *ApJ*, **471**, 352
- Kann, D. A., Agayeva, S., Aivazyan, V., et al. 2023, *ApJ*, **948**, L12
- Kobayashi, S., Piran, T., & Sari, R. 1997, *ApJ*, **490**, 92
- Kumar, R., Carroll, C., Hartikainen, A., & Martin, O. 2019, *The Journal of Open Source Software*, **4**, 1143
- Lamb, G. P., Lyman, J. D., Levan, A. J., et al. 2019, *ApJ*, **870**, L15
- Laskar, T., Alexander, K. D., Margutti, R., et al. 2023, *ApJ*, **946**, L23
- Lattimer, J. M. & Schramm, D. N. 1974, *ApJ*, **192**, L145
- LHAASO Collaboration. 2023, *Science*, **380**, 1390
- MAGIC Collaboration, Acciari, V. A., Ansoldi, S., et al. 2019a, *Nature*, **575**, 455
- MAGIC Collaboration, Acciari, V. A., Ansoldi, S., et al. 2019b, *Nature*, **575**, 459
- Makhathini, S., Mooley, K. P., Brightman, M., et al. 2021, *ApJ*, **922**, 154
- Matsumoto, T., Nakar, E., & Piran, T. 2019, *MNRAS*, **483**, 1247
- McKinney, W. 2010, in *Proceedings of the 9th Python in Science Conference*, ed. S. van der Walt & J. Millman, 56–61
- Mochkovitch, R., Daigne, F., Duque, R., & Zitouni, H. 2021, *A&A*, **651**, A83
- Mooley, K. P., Anderson, J., & Lu, W. 2022, *Nature*, **610**, 273
- Mooley, K. P., Deller, A. T., Gottlieb, O., et al. 2018, *Nature*, **561**, 355
- Murase, K., Toma, K., Yamazaki, R., & Mészáros, P. 2011, *ApJ*, **732**, 77
- Nakar, E. 2007, *Phys. Rep.*, **442**, 166
- Nakar, E., Ando, S., & Sari, R. 2009, *ApJ*, **703**, 675
- Nakar, E. & Piran, T. 2011, *Nature*, **478**, 82
- Nakar, E. & Piran, T. 2018, *MNRAS*, **478**, 407
- Nakar, E. & Piran, T. 2021, *ApJ*, **909**, 114
- O'Connor, B., Troja, E., Ryan, G., et al. 2023, *Science Advances*, **9**, eadi1405
- Oganesyan, G., Ascenzi, S., Branchesi, M., et al. 2020, *ApJ*, **893**, 88
- Palmese, A., Hartley, W., Tarsitano, F., et al. 2017, *ApJ*, **849**, L34
- Panaitescu, A. & Kumar, P. 2000, *ApJ*, **543**, 66
- Piran, T. & Nakar, E. 2010, *ApJ*, **718**, L63
- Rhoads, J. E. 1997, *ApJ*, **487**, L1
- Ryan, G., van Eerten, H., Piro, L., & Troja, E. 2020, *ApJ*, **896**, 166
- Salafia, O. S., Berti, A., Covino, S., et al. 2022a, in *37th International Cosmic Ray Conference*, 944
- Salafia, O. S., Ravasio, M. E., Yang, J., et al. 2022b, *ApJ*, **931**, L19
- Sari, R. & Esin, A. A. 2001, *ApJ*, **548**, 787
- Sari, R., Piran, T., & Narayan, R. 1998, *ApJ*, **497**, L17
- Sato, Y., Murase, K., Ohira, Y., & Yamazaki, R. 2023, *MNRAS*, **522**, L56
- Savchenko, V., Ferrigno, C., Kuulkers, E., et al. 2017, *ApJ*, **848**, L15
- Sedov, L. I. 1946, *Journal of Applied Mathematics and Mechanics*, **10**, 241
- Sironi, L., Keshet, U., & Lemoine, M. 2015, *Space Sci. Rev.*, **191**, 519
- Suda, T., Katsuta, Y., Yamada, S., et al. 2008, *PASJ*, **60**, 1159
- Tanvir, N. R., Levan, A. J., González-Fernández, C., et al. 2017, *ApJ*, **848**, L27
- Taylor, G. 1950, *Proceedings of the Royal Society of London Series A*, **201**, 159
- Troja, E., O'Connor, B., Ryan, G., et al. 2022, *MNRAS*, **510**, 1902
- Troja, E., van Eerten, H., Ryan, G., et al. 2019, *MNRAS*, **489**, 1919
- Troja, E., van Eerten, H., Zhang, B., et al. 2020, *MNRAS*, **498**, 5643
- Uhm, Z. L. & Beloborodov, A. M. 2007, *ApJ*, **665**, L93
- van Eerten, H., van der Horst, A., & MacFadyen, A. 2012, *ApJ*, **749**, 44
- van Eerten, H. J. & MacFadyen, A. I. 2012, *ApJ*, **747**, L30
- Vangioni, E., Goriely, S., Daigne, F., François, P., & Belczynski, K. 2016, *MNRAS*, **455**, 17
- Villar, V. A., Guillochon, J., Berger, E., et al. 2017, *ApJ*, **851**, L21
- Virtanen, P., Gommers, R., Oliphant, T. E., et al. 2020, *Nature Methods*, **17**, 261
- Wang, H., Dastidar, R. G., Giannios, D., & Duffell, P. C. 2024, *ApJS*, **submitted**, arXiv:2402.19359
- Wang, X.-Y., Liu, R.-Y., Zhang, H.-M., Xi, S.-Q., & Zhang, B. 2019, *ApJ*, **884**, 117
- Warren, D. C., Dainotti, M., Barkov, M. V., et al. 2022, *ApJ*, **924**, 40
- Woods, E. & Loeb, A. 1999, *ApJ*, **523**, 187
- Yamasaki, S. & Piran, T. 2022, *MNRAS*, **512**, 2142
- Zhang, B., Wang, X.-Y., & Zheng, J.-H. 2024, *Journal of High Energy Astrophysics*, **41**, 42
- Zheng, J.-H., Wang, X.-Y., Liu, R.-Y., & Zhang, B. 2024, *ApJ*, **966**, 141

Appendix A: Maximum electron Lorentz factor and synchrotron burnoff limit

The maximum Lorentz factor γ_{\max} of accelerated electrons is defined in Section 2.3 and is reached when the acceleration timescale becomes longer than the cooling timescale, i.e.

$$t_{\text{acc}}(\gamma_{\max}) = \min(t_{\text{rad}}(\gamma_{\max}); t_{\text{dyn}}), \quad (\text{A.1})$$

where the dynamical timescale t_{dyn} and the acceleration timescale t_{acc} are defined by Equations (16) and (24). From Equations (38–39), the radiative timescale t_{rad} is given by

$$t_{\text{rad}}(\gamma) = \frac{t_{\text{dyn}}}{1 + Y(\gamma)} \frac{\gamma_c^{\text{syn}}}{\gamma}. \quad (\text{A.2})$$

Equation (A.1) can then be rewritten

$$\min \left[1; \frac{\gamma_c^{\text{syn}}}{\gamma_{\max}(1 + Y(\gamma_{\max}))} \right] = \tilde{K} \gamma_{\max}, \quad (\text{A.3})$$

with

$$\tilde{K} = K_{\text{acc}} \frac{m_e c}{e B t_{\text{dyn}}}. \quad (\text{A.4})$$

Then γ_{\max} is the solution of

$$\gamma_{\max}^2 [1 + Y(\gamma_{\max})] = \frac{\gamma_c^{\text{syn}}}{\tilde{K}} \quad (\text{A.5})$$

except in unlikely cases where electrons at γ_{\max} are slow cooling ($\gamma_{\max} < \gamma_c$), that lead to $\gamma_{\max} = 1/\tilde{K}$.

In the present version of the model, we assume $\gamma_{\max} \gg \gamma_m$ so that the calculation of γ_c and the identification of the radiative regime and associated normalized electron distribution $f(x)$ and Compton parameter $h(x)$ are independent of γ_{\max} (see § 2.4.6). Therefore the maximum Lorentz factor is determined once this radiative regime is identified. We follow an iterative procedure where the segments of $h(x)$ are explored successively starting from the last segment $x > \hat{x}_1$ (highest Lorentz factors):

1. We check if there is a solution of Equation (A.5) in this segment, with the usual approximation for $1 + Y$, i.e.

$$\frac{\gamma_c^{\text{syn}}}{\tilde{K}} = \begin{cases} \gamma_{\max}^2 & \text{if } Y(\gamma_{\max}) < 1 \\ \gamma_{\max}^2 Y(\gamma_{\max}) & \text{if } Y(\gamma_{\max}) > 1 \end{cases}, \quad (\text{A.6})$$

where $Y(\gamma_{\max})$ is computed from Equation (62), which leads to

$$Y(\gamma_{\max}) = \begin{cases} A \frac{\gamma_m}{\gamma_{\text{syn}}} \frac{I_2}{I_0} h(x_{\max}) & \text{if } \gamma_m > \gamma_c \\ A \frac{\gamma_c^{\text{syn}}}{\gamma_m} \frac{I_2}{I_0} h(x_{\max}) & \text{if } \gamma_m < \gamma_c \\ & \text{and } Y(\gamma_{\max}) < 1 \\ \left(A \frac{\gamma_c^{\text{syn}}}{\gamma_m} \frac{I_2}{I_0} h(x_{\max}) \right)^{1/3} & \text{if } \gamma_m < \gamma_c \\ & \text{and } Y(\gamma_{\max}) > 1 \end{cases}. \quad (\text{A.7})$$

The pre-factor A is the same as in Equation (66).

2. If there is a solution in the considered segment, we stop the iterative procedure and keep the following value for the maximum electron Lorentz factor:
 - the solution γ_{\max} found in the segment if $\gamma_{\max} > \gamma_c$ (fast cooling);

- the solution $\gamma_{\max} = 1/\tilde{K}$ otherwise (slow cooling).
3. If there is no solution in the considered segment:
 - If the next segment is still at least partially in fast cooling regime (i.e. the upper bound is above γ_c), we start a new iteration at step 1. using this new segment;
 - otherwise we stop the iterative procedure and keep for γ_{\max} the slow cooling solution $\gamma_{\max} = 1/\tilde{K}$.

In most cases, the maximum electron Lorentz factor is large enough to be in fast cooling regime ($\gamma_{\max} > \gamma_c$ so that $t_{\text{rad}}(\gamma_{\max}) < t_{\text{dyn}}$) with a negligible IC cooling ($Y(\gamma_{\max}) < 1$). In this case, the maximum Lorentz factor

$\gamma_{\max} = \sqrt{\gamma_c^{\text{syn}}/\tilde{K}}$ leads to the usual synchrotron burnoff limit (see e.g. Piran & Nakar 2010) for the high-frequency cutoff of the synchrotron spectrum in the comoving frame $h\nu_{\max} = h\nu_{\text{syn}}(\gamma_{\max}) = K_2 B \gamma_c^{\text{syn}}/\tilde{K}$:

$$h\nu_{\max} = \frac{1}{K_{P_{\max}} \frac{3he^2}{\sigma_T m_e c} K_{\text{acc}}} = \frac{160 \text{ MeV}}{K_{P_{\max}} K_{\text{acc}}}. \quad (\text{A.8})$$

For the best-fit parameters of the afterglow of GW 170817 presented in Section 4, the Lorentz factor of the core jet at t_{peak} is $\Gamma \simeq 10$. The limit is thus expected at ~ 1 GeV in the observer frame, as seen in Fig. 9.

Appendix B: Radiative regimes and corresponding electron distributions

The IC cooling impacts the distribution of electrons if $\max(\gamma_c; \hat{\gamma}_p) < \gamma < \gamma_0$ (Equation (65)). As

$$\hat{\gamma} = \frac{\gamma_{\text{self}}^3}{\gamma^2}, \quad (\text{B.1})$$

all possible cases regarding the radiative regime and the distribution of electrons can be identified in the $(\gamma_{\text{self}}; \gamma_0)$ plane shown in Fig. B.1. As an electron of Lorentz factor γ can upscatter its own synchrotron photon only if $\gamma \leq \hat{\gamma}$, i.e. $\gamma \leq \gamma_{\text{self}}$, the x-axis quantifies the importance of the KN suppression: the lower γ_{self} (left side of the diagram), the more electrons are affected by KN effects. The y-axis quantifies the importance of IC cooling: the IC power of all electrons with $\gamma > \gamma_0$ is negligible compared to the synchrotron power. Therefore, the lower γ_0 (bottom of the diagram), the more electrons have a negligible IC cooling. We list in Tables B.1 (fast cooling) and B.2 (slow cooling) all these cases and provide the corresponding self-consistent solution (breaks and slopes) for the normalized distribution of electrons $f(x)$ (Equation (43)) and the normalized Compton parameter $h(x)$ (Equation (62)), as obtained following the detailed method described in Nakar et al. (2009). The break corresponding to the peak of the synchrotron spectrum is highlighted in red. We also provide in each case the expression of γ_0 obtained from the relation $Y(\gamma_c) = h(x_c)/h(x_0)$ (Equation (67)), as needed in the iterative procedure to determine $Y(\gamma_c)$: see § 2.4.6.

The distribution of electrons is unaffected by the SSC cooling when $\gamma_0 < \gamma_c$ or $\gamma_c < \gamma_0 < \hat{\gamma}_{m,c}$. These two regions are shaded in orange and blue in Fig. B.1. When $\gamma_0 < \hat{\gamma}_{m,c}$ (cases F1 and S1), the IC cooling is negligible for all electrons and γ_0 is undefined. The solution is provided by the pure synchrotron case (§ 2.4.4). When $\hat{\gamma}_{m,c} < \gamma_0 < \gamma_c$

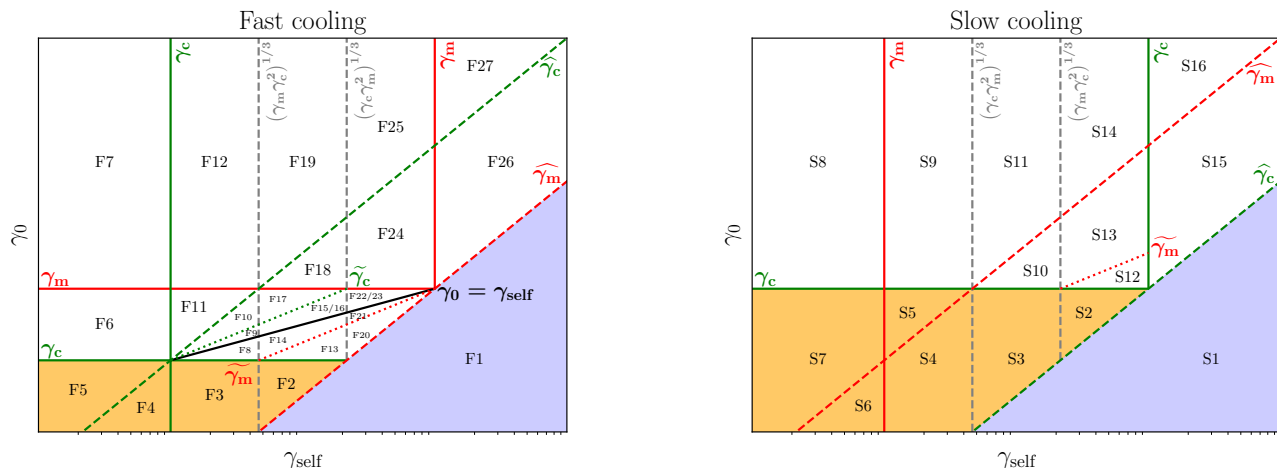


Fig. B.1. Definition of all possible cases for the radiative regime and the distribution of electrons in the plane γ_0 vs γ_{self} . The Lorentz factors γ_m and γ_c are indicated by red and green solid lines either in the fast cooling regime with $\gamma_m > \gamma_c$ (left) or in the slow cooling regime with $\gamma_m < \gamma_c$ (right). The black solid line in the left panel corresponds to $\gamma_0 = \gamma_{\text{self}}$. The two Lorentz factors $\hat{\gamma}_m$ (red) and $\hat{\gamma}_c$ (green) are plotted in dashed lines. In some regions, additional Lorentz factors relevant to identify the radiative regime are also plotted: $\tilde{\gamma}_m$ (red dotted line) and $\tilde{\gamma}_c$ (green dotted line). The regions where there is no impact of the SSC cooling on the distribution of electrons are shaded in orange ($\hat{\gamma}_{m,c} < \gamma_0 < \gamma_c$) and blue ($\gamma_0 < \hat{\gamma}_{m,c}$). This diagram allows to identify all possible orderings of γ_0 , γ_m , γ_c , $\hat{\gamma}_m$, $\hat{\gamma}_c$ defining all possible radiative regimes. The corresponding limits for γ_{self} are indicated by vertical black dashed lines. All the possible cases are listed in Table B.1 (fast cooling) and B.2 (slow cooling). In practice, several cases have the same breaks and slopes for $f(x)$ and $h(x)$ and can therefore be treated simultaneously in the numerical implementation of the model. This allows to group (F1, F2, F3, F4, F5), (F8, F13, F14), (F9, F15, F16), (F10, F17), (F20, F21), (F22, F23), (S1, S2, S3, S4, S5, S6, S7), (S8, S9), (S10, S12, S13) and (S11, S14).

(cases F2 to F5 and S2 to S6), the normalized electron distribution $f(x)$ is also the same as in the pure synchrotron case but γ_0 is defined and its expression depends on the considered regime.

In all other cases, the SSC cooling affects the distribution of electrons and the synchrotron spectrum, with additional breaks ($N \geq 3$), as listed in Tables B.1 and B.2. There are more subcases in fast cooling. The most relevant ones for GRB afterglows are discussed in Nakar et al. (2009): their case I with its two subcases correspond to F26 and F27; their case IIa to F20-F21, their case IIb to F22-F23; their cases IIc and III to some subcases of F24 and F25.

Cases F24 and F25 are indeed more complex and require a specific treatment (see Section 3.2 Nakar et al. 2009), as a large number of breaks can appear in the distribution, that must be found iteratively. These two cases correspond to $\gamma_c < \hat{\gamma}_m < \gamma_{\text{self}} < \gamma_m < \hat{\gamma}_c$. New breaks will appear in the spectral shape $f(x)$ every time that $^{(2n)}\hat{\gamma}_m = \hat{\gamma}_c$, where using Equation (B.1), we define the successive $^{(n)}\hat{\gamma}$ as

$$^{(n)}\hat{\gamma} = \begin{cases} \frac{\gamma_{\text{self}}^{2^{n+1}}}{\gamma_{\text{self}}^{2^n}} & \text{if } n \text{ is odd} \\ \frac{\gamma_{\text{self}}^{2^n}}{\gamma_{\text{self}}^{2^{n-1}}} & \text{if } n \text{ is even} \end{cases} \quad (\text{B.2})$$

This condition is equivalent to $\gamma_{\text{self}} = \gamma_{\text{self,cr},2n}$, where

$$\gamma_{\text{self,cr},2n} = \left(\gamma_m^{2^{2n-1}} \gamma_c \right)^{\frac{1}{2^{2n-1}+1}}, \quad (\text{B.3})$$

with $n \geq 1$. For $n = 1$, the first value $\gamma_{\text{self,cr},2} = (\gamma_m^2 \gamma_c)^{\frac{1}{3}}$ is plotted in Fig. B.1 and is the frontier at low γ_{self} of the cases F24 and F25. On the other hand $\gamma_{\text{self,cr},2n}$ tends to γ_m when n tends to infinity, i.e. the frontier at high γ_{self} . Then, the values of $\gamma_{\text{self,cr},2n}$ for $n > 1$ divide F24 and F25 in many sub-regions. We define the column n by

the condition $\gamma_{\text{self,cr},2n} < \gamma_{\text{self}} < \gamma_{\text{self,cr},2n+2}$. In practice, $\gamma_{\text{self,cr},2n}$ rapidly converges, and the spectral shapes in these narrower columns rapidly become closer and closer to each other. This allows numerically to not distinguish columns above a certain n_{max} . We use $n_{\text{max}} = 7$.

In each column n , cases F24 and F25 are then divided in several subcases depending on the relative position of γ_0 and $\tilde{\gamma}_c$, $\hat{\gamma}_c$ and $^{(2k)}\hat{\gamma}_m$ with $k \geq 1$. In each subcase, the list of breaks and slopes can be determined for $f(x)$ and $h(x)$, as well as the position of the peak of the synchrotron spectrum. We show for illustration the results in the two first columns in Table B.3.

Appendix C: Posterior distributions of the three fits of the afterglow of GW 170817

Fig. B.2 gives the posterior joint and marginalized distributions of the model parameters for the three fits of the multi-wavelength afterglow of GW 170817 described in Section 4. The three fits use the same observational constraints and the same priors on the free parameters, and differ only by the radiative treatment: synchrotron only ("no SSC"), synchrotron and SSC assuming that all IC scatterings occur in Thomson regime ("SSC (Thomson)"), and self-consistent calculation of synchrotron and SSC processes taking into account the KN attenuation ("SSC (with KN)"). It appears clearly that the "no SSC" and "SSC (with KN)" fits lead to similar results, whereas the parameters inferred by the "SSC (Thomson)" fit are slightly different (see also Table 4). This especially true for the viewing and core jet opening angles, but also for the kinetic energy and the external density. Note the correlations between these quantities. This difference is due to the fact that the SSC component in the afterglow of GW 170817 is very weak due to the KN attenuation, and is therefore overestimated in the "SSC (Thomson)" case: see discussion in § 4.3.

Table B.1. Fast cooling: list of all possible radiative regimes and corresponding electron distribution.

Case F1	breaks	γ_c	$\hat{\gamma}_m$	$\hat{\gamma}_c$	$\hat{\gamma}_c$				γ_0 undefined
	f slopes	2			$p+1$				
	h slopes	0			$1/2$		$4/3$		
Case F2	breaks	$\hat{\gamma}_m$	γ_0	γ_c	$\hat{\gamma}_m$	$\hat{\gamma}_c$			$\gamma_0 = \gamma_c Y_c^2$
	f slopes			2		$p+1$			
	h slopes	0		$1/2$			$4/3$		
Case F3	breaks	$\hat{\gamma}_m$	γ_0	γ_c	$\hat{\gamma}_c$	$\hat{\gamma}_m$	$\hat{\gamma}_c$		$\gamma_0 = \gamma_c Y_c^2$
	f slopes				2		$p+1$		
	h slopes	0		$1/2$			$4/3$		
Case F4	breaks	$\hat{\gamma}_m$	γ_0	$\hat{\gamma}_c$	γ_c	$\hat{\gamma}_m$	$\hat{\gamma}_c$		$\gamma_0 = \gamma_c^{8/3} \hat{\gamma}_c^{-5/3} Y_c^2$
	f slopes				2		$p+1$		
	h slopes	0		$1/2$			$4/3$		
Case F5	breaks	$\hat{\gamma}_m$	$\hat{\gamma}_c$	γ_0	γ_c	$\hat{\gamma}_m$	$\hat{\gamma}_c$		$\gamma_0 = \gamma_c Y_c^{3/4}$
	f slopes				2		$p+1$		
	h slopes	0	$1/2$			$4/3$			
Case F6	breaks	$\hat{\gamma}_m$	$\hat{\gamma}_0$	$\hat{\gamma}_c$	γ_c	γ_0	$\hat{\gamma}_m$	$\hat{\gamma}_c$	$\gamma_0 = \gamma_c Y_c^{3/4}$
	f slopes					$2/3$	2	$p+1$	
	h slopes	0	$1/2$	$7/6$			$4/3$		
Case F7	breaks	$\hat{\gamma}_0$	$\hat{\gamma}_m$	$\hat{\gamma}_c$	γ_c	γ_m	$\hat{\gamma}_0$	$\hat{\gamma}_c$	$\gamma_0 = \gamma_c Y_c^{3/4}$
	f slopes					$2/3$	$p-1/3$	$p+1$	
	h slopes	0	$(10-3p)/6$	$7/6$			$4/3$		
Case F8	breaks	$\hat{\gamma}_m$	γ_c	γ_0	$\hat{\gamma}_0$	$\hat{\gamma}_c$	$\hat{\gamma}_m$	$\hat{\gamma}_c$	$\gamma_0 = \gamma_c Y_c^2$
	f slopes		$3/2$		2		$p+1$		
	h slopes	0	$1/2$		$3/4$		$4/3$		
Case F9	breaks	$\hat{\gamma}_m$	γ_c	$\hat{\gamma}_0$	γ_0	$\hat{\gamma}_0$	$\hat{\gamma}_c$	$\hat{\gamma}_m$	$\gamma_0 = \gamma_c^{1/2} \hat{\gamma}_0^{1/2} Y_c = \gamma_c^{1/4} \gamma_{\text{self}}^{3/4} Y_c^{1/2}$
	f slopes		$3/2$	1	γ_0	2		$p+1$	
	h slopes	0	$1/2$		1		$3/4$	$4/3$	
Case F10	breaks	$\hat{\gamma}_m$	$\hat{\gamma}_0$	γ_c	γ_0	$\hat{\gamma}_c$	$\hat{\gamma}_m$	$\hat{\gamma}_c$	$\gamma_0 = \gamma_c Y_c$
	f slopes				1		$p+1$		
	h slopes	0	$1/2$		1		$4/3$		
Case F11	breaks	$\hat{\gamma}_m$	$\hat{\gamma}_0$	$\hat{\gamma}_c$	γ_c	$\hat{\gamma}_c$	γ_0	$\hat{\gamma}_m$	$\gamma_0 = \gamma_c^{3/4} \hat{\gamma}_c^{1/4} Y_c^{3/4}$
	f slopes					1	$2/3$	2	
	h slopes	0	$1/2$	$7/6$		1		$4/3$	
Case F12	breaks	$\hat{\gamma}_0$	$\hat{\gamma}_m$	$\hat{\gamma}_c$	γ_c	$\hat{\gamma}_c$	γ_m	$\hat{\gamma}_0$	$\gamma_0 = \gamma_c^{3/4} \hat{\gamma}_c^{1/4} Y_c^{3/4}$
	f slopes					1	$2/3$	$p-1/3$	
	h slopes	0	$(10-3p)/6$	$7/6$		1		$4/3$	
Case F13	breaks	$\hat{\gamma}_m$	γ_c	γ_0	$\hat{\gamma}_0$	$\hat{\gamma}_c$	$\hat{\gamma}_m$	$\hat{\gamma}_c$	$\gamma_0 = \gamma_c Y_c^2$
	f slopes		$3/2$		2		$p+1$		
	h slopes	0	$1/2$		$3/4$		$4/3$		
Case F14	breaks	$\hat{\gamma}_m$	γ_c	γ_0	$\hat{\gamma}_m$	$\hat{\gamma}_c$	$\hat{\gamma}_0$	$\hat{\gamma}_c$	$\gamma_0 = \gamma_c Y_c^2$
	f slopes		$3/2$	2			$p+1$		
	h slopes	0	$1/2$		$3/4$		$4/3$		
Case F15	breaks	$\hat{\gamma}_m$	γ_c	$\hat{\gamma}_0$	γ_0	$\hat{\gamma}_0$	$\hat{\gamma}_c$	$\hat{\gamma}_m$	$\gamma_0 = \gamma_c^{1/2} \hat{\gamma}_0^{1/2} Y_c = \gamma_c^{1/4} \gamma_{\text{self}}^{3/4} Y_c^{1/2}$
	f slopes		$3/2$	1	γ_0	2		$p+1$	
	h slopes	0	$1/2$		1		$3/4$	$4/3$	
Case F16	breaks	$\hat{\gamma}_m$	γ_c	$\hat{\gamma}_0$	γ_0	$\hat{\gamma}_m$	$\hat{\gamma}_c$	$\hat{\gamma}_0$	$\gamma_0 = \gamma_c^{1/2} \hat{\gamma}_0^{1/2} Y_c = \gamma_c^{1/4} \gamma_{\text{self}}^{3/4} Y_c^{1/2}$
	f slopes		$3/2$	1	γ_0	2		$p+1$	
	h slopes	0	$1/2$		1		$3/4$	$4/3$	
Case F17	breaks	$\hat{\gamma}_m$	$\hat{\gamma}_0$	γ_c	γ_0	$\hat{\gamma}_m$	$\hat{\gamma}_c$	$\hat{\gamma}_0$	$\gamma_0 = \gamma_c Y_c$
	f slopes				1	2		$p+1$	
	h slopes	0	$1/2$		1		$4/3$		
Case F18	breaks	$\hat{\gamma}_0$	$\hat{\gamma}_m$	γ_c	γ_m	$\hat{\gamma}_0$	$\hat{\gamma}_c$	$\hat{\gamma}_m$	$\gamma_0 = \gamma_c Y_c$
	f slopes				1	p		$p+1$	
	h slopes	0	$(3-p)/2$		1		$4/3$		
Case F19	breaks	$\hat{\gamma}_0$	$\hat{\gamma}_c$	$\hat{\gamma}_m$	γ_c	γ_m	$\hat{\gamma}_c$	$\hat{\gamma}_0$	$\gamma_0 = \gamma_c^{3/4} \hat{\gamma}_c^{1/4} Y_c^{3/4}$
	f slopes					1	p	$p-1/3$	
	h slopes	0	$(10-3p)/6$	$(3-p)/2$		1		$4/3$	
Case F20	breaks	γ_c	$\hat{\gamma}_m$	γ_0	$\hat{\gamma}_0$	$\hat{\gamma}_m$	$\hat{\gamma}_c$	$\hat{\gamma}_0$	$\gamma_0 = \hat{\gamma}_m Y_c^2$
	f slopes	2		$3/2$	2		$p+1$		
	h slopes	0		$1/2$		$3/4$	$1/2$	$4/3$	
Case F21	breaks	γ_c	$\hat{\gamma}_m$	γ_0	$\hat{\gamma}_m$	$\hat{\gamma}_c$	$\hat{\gamma}_0$	$\hat{\gamma}_c$	$\gamma_0 = \hat{\gamma}_m Y_c^2$
	f slopes	2		$3/2$	2		$p+1$		
	h slopes	0		$1/2$		$3/4$	$1/2$	$4/3$	
Case F22	breaks	γ_c	$\hat{\gamma}_m$	$\hat{\gamma}_0$	γ_0	$\hat{\gamma}_0$	$\hat{\gamma}_m$	$\hat{\gamma}_c$	$\gamma_0 = \hat{\gamma}_m^{1/2} \hat{\gamma}_0^{1/2} Y_c = \hat{\gamma}_m^{1/4} \gamma_{\text{self}}^{3/4} Y_c^{1/2}$
	f slopes	2		$3/2$	1	2		$p+1$	
	h slopes	0		$1/2$	1		$3/4$	$1/2$	
Case F23	breaks	γ_c	$\hat{\gamma}_m$	$\hat{\gamma}_0$	γ_0	$\hat{\gamma}_m$	$\hat{\gamma}_c$	$\hat{\gamma}_0$	$\gamma_0 = \hat{\gamma}_m^{1/2} \hat{\gamma}_0^{1/2} Y_c = \hat{\gamma}_m^{1/4} \gamma_{\text{self}}^{3/4} Y_c^{1/2}$
	f slopes	2		$3/2$	1	2		$p+1$	
	h slopes	0		$1/2$	1		$3/4$	$1/2$	
Case F26	breaks	γ_c	$\hat{\gamma}_m$	$\hat{\gamma}_c$	γ_0	$\hat{\gamma}_c$	$\hat{\gamma}_m$	$\hat{\gamma}_c$	$\gamma_0 = \hat{\gamma}_m Y_c^2$
	f slopes	2		$p+1$	$p+1/2$		$p+1$		
	h slopes	0		$1/2$		$4/3$			
Case F27	breaks	γ_c	$\hat{\gamma}_m$	$\hat{\gamma}_c$	γ_0	$\hat{\gamma}_c$	$\hat{\gamma}_m$	$\hat{\gamma}_c$	$\gamma_0 = \hat{\gamma}_m^{3/8} \hat{\gamma}_c^{5/8} Y_c^{3/4}$
	f slopes	2		$p+1$	$p+1/2$		$p-1/3$	$p+1$	
	h slopes	0		$1/2$		$4/3$			

Notes. For each case, the first row of the table gives the list of breaks appearing either in the normalized electron distribution $f(x)$, i.e. the list of x_i , or in the normalized Compton parameter $h(x)$, i.e. list of relevant \hat{x}_i , as well as all other necessary characteristic Lorentz factors to fully define the case in agreement with Fig. B.1 (blue). The break corresponding to the peak of the synchrotron spectrum is highlighted in red. The second and third rows give the slopes $-d \ln f/d \ln x$ and $-d \ln g/d \ln x$ for each branch. Finally, the last column gives the expression of γ_0 . Cases F24 and F25 require a specific treatment: see text in appendix B.

Table B.2. Slow cooling: list of all possible radiative regimes and corresponding electron distribution.

Case S1	breaks	γ_m	γ_c	$\widehat{\gamma}_c$	$\widehat{\gamma}_m$	γ_0 undefined		
	f slopes	p			$p+1$			
	h slopes	0		$(3-p)/2$	$4/3$			
Case S2	breaks	γ_m	$\widehat{\gamma}_c$	γ_0	γ_c	$\widehat{\gamma}_m$	$\gamma_0 = \gamma_c Y_c^{2/(3-p)}$	
	f slopes		2			$p+1$		
	h slopes	0		$(3-p)/2$		$4/3$		
Case S3	breaks	$\widehat{\gamma}_c$	γ_0	γ_m	γ_0	γ_c	$\widehat{\gamma}_m$	$\gamma_0 = \gamma_c Y_c^{2/(3-p)}$
	f slopes			2			$p+1$	
	h slopes	0		$(3-p)/2$			$4/3$	
Case S4	breaks	$\widehat{\gamma}_c$	γ_0	γ_m	γ_0	$\widehat{\gamma}_m$	γ_c	$\gamma_0 = \gamma_c^{8/(9-3p)} \widehat{\gamma}_m^{(1-3p)/(9-3p)} Y_c^{2/(3-p)}$
	f slopes				2		$p+1$	
	h slopes	0		$(3-p)/2$			$4/3$	
Case S5	breaks	$\widehat{\gamma}_c$	γ_m	$\widehat{\gamma}_m$	γ_0	γ_c		$\gamma_0 = \gamma_c Y_c^{3/4}$
	f slopes				p		$p+1$	
	h slopes	0		$(3-p)/2$			$4/3$	
Case S6	breaks	$\widehat{\gamma}_c$	γ_0	$\widehat{\gamma}_m$	γ_m	γ_c		$\gamma_0 = \gamma_c^{8/(9-3p)} \widehat{\gamma}_m^{(1-3p)/(9-3p)} Y_c^{2/(3-p)}$
	f slopes					p	$p+1$	
	h slopes	0		$(3-p)/2$			$4/3$	
Case S7	breaks	$\widehat{\gamma}_c$	$\widehat{\gamma}_m$	γ_0	γ_m	γ_0	γ_c	$\gamma_0 = \gamma_c Y_c^{3/4}$
	f slopes					p	$p+1$	
	h slopes	0		$(3-p)/2$			$4/3$	
Case S8	breaks	$\widehat{\gamma}_0$	$\widehat{\gamma}_c$	$\widehat{\gamma}_m$	γ_m	γ_c	γ_0	$\gamma_0 = \gamma_c Y_c^{3/4}$
	f slopes					$p-1/3$	$p+1$	
	h slopes	0		$(10-3p)/6$	$(3-p)/2$		$4/3$	
Case S9	breaks	$\widehat{\gamma}_0$	$\widehat{\gamma}_c$	γ_m	$\widehat{\gamma}_m$	γ_c	γ_0	$\gamma_0 = \gamma_c Y_c^{3/4}$
	f slopes				p	$p-1/3$	$p+1$	
	h slopes	0		$(10-3p)/6$	$(3-p)/2$		$4/3$	
Case S10 ($p < 7/3$)	breaks	$\widehat{\gamma}_0$	$\widehat{\gamma}_c$	γ_m	γ_c	γ_0	$\widehat{\gamma}_m$	$\gamma_0 = \gamma_c Y_c^{2/(3-p)}$
	f slopes				p	$(3p-1)/2$	$p+1$	
	h slopes	0		$(7-3p)/4$		$(3-p)/2$	$4/3$	
Case S10 ($p > 7/3$)	breaks	$\widehat{\gamma}_0$	$\widehat{\gamma}_c$	γ_m	γ_c	γ_0	$\widehat{\gamma}_m$	$\gamma_0 = \gamma_c Y_c^{2/(3-p)}$
	f slopes				p	$(3p-1)/2$	$p+1$	
	h slopes	0		$(3-p)/2$			$4/3$	
Case S11 ($p < 7/3$)	breaks	$\widehat{\gamma}_0$	$\widehat{\gamma}_m$	$\widehat{\gamma}_c$	γ_m	γ_c	$\widehat{\gamma}_m$	$\gamma_0 = \widehat{\gamma}_m^{(3p-1)/8} \gamma_c^{(9-3p)/8} Y_c^{3/4}$
	f slopes				p	$(3p-1)/2$	$p-1/3$	
	h slopes	0		$(10-3p)/6$	$(7-3p)/4$	$(3-p)/2$	$4/3$	
Case S11 ($p > 7/3$)	breaks	$\widehat{\gamma}_0$	$\widehat{\gamma}_m$	$\widehat{\gamma}_c$	γ_m	γ_c	$\widehat{\gamma}_m$	$\gamma_0 = \widehat{\gamma}_m^{(3p-1)/8} \gamma_c^{(9-3p)/8} Y_c^{3/4}$
	f slopes				p	$(3p-1)/2$	$p-1/3$	
	h slopes	0		$(3-p)/2$			$4/3$	
Case S12 ($p < 7/3$)	breaks	γ_m	$\widehat{\gamma}_0$	$\widehat{\gamma}_c$	γ_c	γ_0	$\widehat{\gamma}_m$	$\gamma_0 = \gamma_c Y_c^{2/(3-p)}$
	f slopes				p	$(3p-1)/2$	$p+1$	
	h slopes	0		$(7-3p)/4$		$(3-p)/2$	$4/3$	
Case S12 ($p > 7/3$)	breaks	γ_m	$\widehat{\gamma}_0$	$\widehat{\gamma}_c$	γ_c	γ_0	$\widehat{\gamma}_m$	$\gamma_0 = \gamma_c Y_c^{2/(3-p)}$
	f slopes				p	$(3p-1)/2$	$p+1$	
	h slopes	0		$(3-p)/2$			$4/3$	
Case S13 ($p < 7/3$)	breaks	$\widehat{\gamma}_0$	γ_m	$\widehat{\gamma}_c$	γ_c	γ_0	$\widehat{\gamma}_m$	$\gamma_0 = \gamma_c Y_c^{2/(3-p)}$
	f slopes				p	$(3p-1)/2$	$p+1$	
	h slopes	0		$(7-3p)/4$		$(3-p)/2$	$4/3$	
Case S13 ($p > 7/3$)	breaks	$\widehat{\gamma}_0$	γ_m	$\widehat{\gamma}_c$	γ_c	γ_0	$\widehat{\gamma}_m$	$\gamma_0 = \gamma_c Y_c^{2/(3-p)}$
	f slopes				p	$(3p-1)/2$	$p+1$	
	h slopes	0		$(3-p)/2$			$4/3$	
Case S14 ($p < 7/3$)	breaks	$\widehat{\gamma}_0$	$\widehat{\gamma}_m$	γ_m	$\widehat{\gamma}_c$	γ_c	$\widehat{\gamma}_m$	$\gamma_0 = \widehat{\gamma}_m^{(3p-1)/8} \gamma_c^{(9-3p)/8} Y_c^{3/4}$
	f slopes				p	$(3p-1)/2$	$p-1/3$	
	h slopes	0		$(10-3p)/6$	$(7-3p)/4$	$(3-p)/2$	$4/3$	
Case S14 ($p > 7/3$)	breaks	$\widehat{\gamma}_0$	$\widehat{\gamma}_m$	γ_m	$\widehat{\gamma}_c$	γ_c	$\widehat{\gamma}_m$	$\gamma_0 = \widehat{\gamma}_m^{(3p-1)/8} \gamma_c^{(9-3p)/8} Y_c^{3/4}$
	f slopes				p	$(3p-1)/2$	$p-1/3$	
	h slopes	0		$(3-p)/2$			$4/3$	
Case S15	breaks	γ_m	γ_c	$\widehat{\gamma}_c$	γ_0	$\widehat{\gamma}_m$		$\gamma_0 = \gamma_c Y_c^{2/(3-p)}$
	f slopes		$p+1$		$(3p-1)/2$	$p+1$		
	h slopes	0		$(3-p)/2$		$4/3$		
Case S16	breaks	γ_m	γ_c	$\widehat{\gamma}_c$	$\widehat{\gamma}_m$	γ_0		$\gamma_0 = \widehat{\gamma}_m^{(3p-1)/8} \gamma_c^{(9-3p)/8} Y_c^{3/4}$
	f slopes		$p+1$		$(3p-1)/2$	$p-1/3$	$p+1$	
	h slopes	0		$(3-p)/2$		$4/3$		

Notes. Same convention as in table B.1.

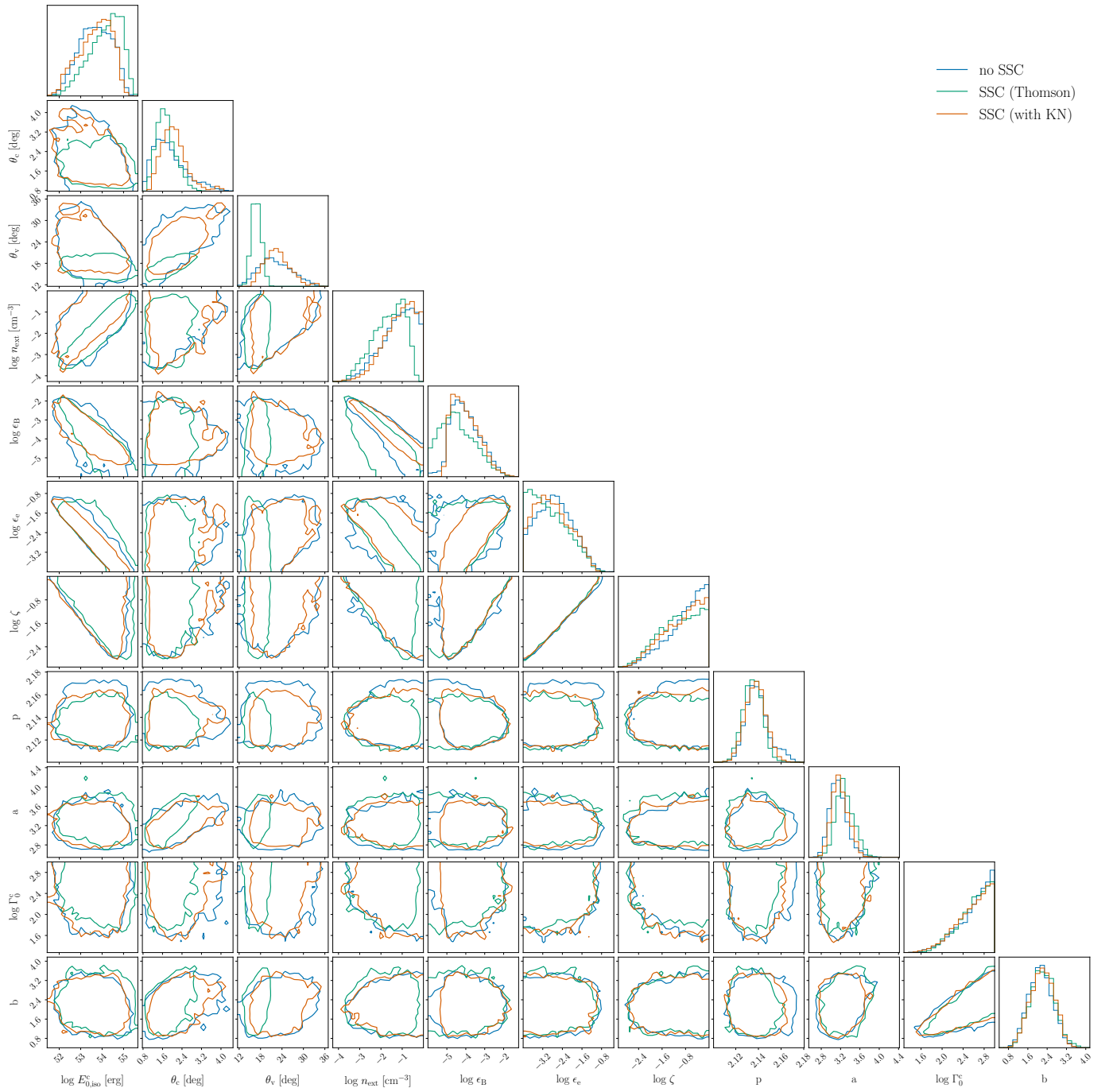


Fig. B.2. Posterior joint and marginalized distributions of the model's free parameters, $E_{0,\text{iso}}^C$, θ_c , θ_v , n_{ext} , ϵ_B , ϵ_e , ζ , p , a , Γ_0^C , b for the three fits of the afterglow of GW 170817 presented in section 4, which differ only by the treatment of the radiative processes: in blue, no SSC diffusions are taken into account ("no SSC"); in green, SSC diffusions are assumed to be only in the Thomson regime ("SSC (Thomson)"); in orange, the SSC diffusion is depleted at high energy in the Klein-Nishina regime ("SSC (with KN)"). The colored contours correspond to the 3σ confidence intervals for each model and each parameter.